THE HONG KONG
POLYTECHNIC UNIVERSITY
香港理工大學
Pao Yue-kong Library
包玉剛圖書館

Copyright Undertaking

This thesis is protected by copyright, with all rights reserved.

By reading and using the thesis, the reader understands and agrees to the following terms:

1. The reader will abide by the rules and legal ordinances governing copyright regarding the use of the thesis.

2. The reader will use the thesis for the purpose of research or private study only and not for distribution or further reproduction or any other purpose.

3. The reader agrees to indemnify and hold the University harmless from and against any loss, damage, cost, liability or expenses arising from copyright infringement or unauthorized usage.

Pao Yue-kong Library, The Hong Kong Polytechnic University, Hung Hom, Kowloon, Hong Kong

http://www.lib.polyu.edu.hk

GROWTH AND CHARACTERIZATION OF TRANSITION METAL TELLURIDE THIN FILMS

CHAN CHEUK HO

MPhil

The Hong Kong Polytechnic University

2019

The Hong Kong Polytechnic University

Department of Applied Physics

GROWTH AND CHARACTERIZATION OF TRANSITION METAL TELLURIDE THIN FILMS

CHAN CHEUK HO

A thesis submitted in partial fulfillment of the requirements for

the degree of

Master of Philosophy

June 2018

CERTIFICATE OF ORIGINALITY

I hereby declare that this thesis is my own work and that, to the best of my knowledge and belief, it reproduces no material previously published or written, nor material that has been accepted for the award of any other degree or diploma, except where due acknowledgment has been made in the text.

_____   _____ (Signed)

_____ CHAN Cheuk Ho _____ (Name of student)

ABSTRACT

Transition metal tellurides have attracted great deal of interests due to their non-trivial band structure leading to non-trivial electronic behaviors. As a member of the transition metal dichalcogenides (TMDs) family, zirconium tellurides have shown topological semimetal and Dirac fermion characteristics. In this project, the zirconium ditelluride thin films have been deposited on different substrates by pulsed laser deposition (PLD) system. It is found that the thin film quality can be well controlled by adjusting the deposition conditions such as substrate temperature. It is also found that the zirconium ditelluride thin films are extremely unstable under ambient atmosphere, therefore, tellurium and polycrystalline aluminum nitride (AlN) are used as capping layer to protect the thin films from reaction with moisture and air.

Microstructure and crystallographic orientation of $ZrTe_2$ thin films are characterized by x-ray diffraction (XRD) and transmission electron microscopy (TEM). The results reveal that within a range of growth temperatures from 500 ºC to 750 ºC, the hexagonal $ZrTe_2$ thin films are epitaxially grown on (0001) sapphire substrate with high quality and uniformity; while the crystalline quality of thin films decreases as the grown temperature is decreased. The thicknesses of the $ZrTe_2$ thin films are about 60 nm and there is no interfacial layer between the film and substrate. The orientation relationship of the film and substrate is $(0001)_{ZrTe2}//(0001)_s$ and $[11\bar{2}0]_{ZrTe2}//[01\bar{1}0]_s$.

For the $ZrTe_2$ thin films grown on (110) STO substrates, the main growth orientation is also along its [0001] direction, but the films present more defects and grains. There is also an interfacial layer of about 5 nm thick. This interfacial layer could be $ZrTe_2$ but with a different growth orientation along $[01\bar{1}1]$ direction or a different phase such as ZrTe.

The dominant growth orientation along [0001] is attributed to the layered structure of $ZrTe_2$.

Electrical transport properties of the $ZrTe_2$ films are characterized by a 9T-PPMS (Physical Property Measurement System) from Quantum Design. The $ZrTe_2$ thin film on sapphire substrate presents metallic transport characteristics within temperature range from 300 K to 2 K, and weak magnetoresistance can also be observed.

The thin film on STO (110) substrate also show typical R-T behavior of a metal or semi-metal, but with much larger change of resistance from room temperature to 2K. Moreover, large magnetoresistance is observed in the films when an external magnetic field is applied perpendicular to the film plane; while parallel magnetic field results in negative MR. More evidences suggest that the $ZrTe_2$ film on (110) STO substrate could be topological semimetal.

LIST OF PUBLICATIONS

Journal Publication

[1]   T. Zhang, Z. Zhang, <u>C. H. Chan</u>, L. Li, M. L. Wei, X. Meng, J. Y. Dai, X. Y. Qiu, "Visible-light enhanced charge storage characteristics of amorphous Ni-doped HfO_2 films," *Journal of Physics D: Applied Physics,* 2018.

[2]   Z. Zhang, J. Qian, W. Lu, <u>C. H. Chan</u>, S. P. Lau, and J. Y. Dai, "In situ TEM study of the sodiation/desodiation mechanism of MnO_2 nanowire with gel-electrolytes," *Energy Storage Materials,* vol. 15, pp. 91-97, 2018.

[3]   W. Z.. Liang, M. Gao, C. Lu, Z. Zhang, <u>C. H. Chan</u>, L. J. Zhuge, J. Y. Dai, H. Yang, C. L. Chen, B. H. Park, "Enhanced Metal–Insulator Transition Performance in Scalable Vanadium Dioxide Thin Films Prepared Using a Moisture-Assisted Chemical Solution Approach," *ACS applied materials & interfaces,* vol. 10, no. 9, pp. 8341-8348, 2018

[4]   Z. Zhang, F. Zhang, H. C. Wang, <u>C. H. Chan</u>, W. Lu, and J. Y. Dai, "Substrate orientation-induced epitaxial growth of face centered cubic Mo_2C superconductive thin film," *Journal of Materials Chemistry C,* vol. 5, no. 41, pp. 10822-10827, 2017.

[5]   F. Zhang, Z. Zhang, H. C. Wang, <u>C. H. Chan</u>, N. Y. Chan, X. X. Chen, J. Y. Dai, "Plasma-enhanced pulsed-laser deposition of single-crystalline Mo_2C ultrathin superconducting films," *Physical Review Materials,* vol. 1, no. 3, p. 034002, 2017.

[6]   C. H. Suen, D. L. Shi, Y. Su, Z. Zhang, <u>C. H. Chan</u>, X. D. Tang, Y. Li, K. H. Lam, X. X. Chen, B. L. Huang, X. Y. Zhou, J. Y. Dai, "Enhanced thermoelectric properties of SnSe thin films grown by pulsed laser glancing-angle deposition," *Journal of Materiomics,* vol. 3, no. 4, pp. 293-298, 2017.

[7]   X. Y. Qiu, R. X. Wang, G. Q. Li, T. Zhang, L. T. Li, M. L. Wei, X. S. Meng, H. Ji, Z. Zhang, <u>C. H. Chan</u>, "Oxygen-dependent epitaxial growth of Pt (001) thin films on MgO (001) by magnetron sputtering," *Applied Surface Science,* vol. 406, pp. 212-217, 2017.

ACKNOWLEDGEMENTS

TABLE OF CONTENTS

LIST OF FIGURES

LIST OF TABLES

CHAPTER 1 INTRODUCTION

1.1 Brief introduction

Two-Dimensional Transition Metal Dichalcogenide (2D TMDs), a sub-group of 2D materials, have been extensively studied for serval years showing extraordinary properties for variety of applications. For example, the van der Waals gap between each layer and the large surface area sheet-like structures benefiting the ion intercalation or electron accumulation, which make 2D TMDs a promising electrode materials for batteries and supercapacitors. [1] For example, the MoS_2 biosensor shows rapid response, high sensitivity and low recovery power consumption because of its high surface-to-volume ratio and the sheet-like structures of 2D TMDs. [2] The van der Waals (vdW) bonding between 2D TMDs atomic layers not only make the mechanical exfoliation of 2D TMDs possible, but also creates a novel way for synthesizing and engineering vdW heterostructures by isolating and stacking with others TMDs. [3] Several researchers conducted the study of engineering vdW heterostructures, such as the band alignment and interlayer coupling for electronic and optoelectronic devices. [4] Besides, 2D TMDs are used in different aspects of devices due to their irreplaceable chemical, physical and opto-electronic properties. [5]
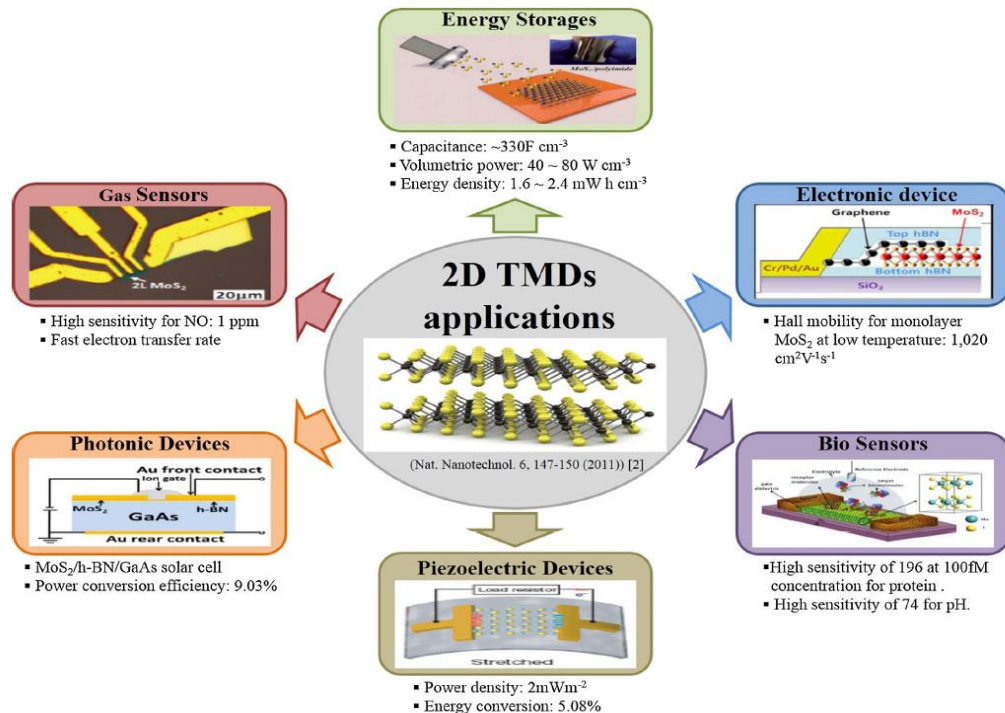
Figure 1-1 2D TMDs based devices in different aspects. [5]

As a member of TMDs family, transition metal ditellurides share some special properties such as high stability in low-dimensional structure, intrinsic non-trivial band structure and wide application in electronic devices. Besides, some transition metal telluride compounds crystallized as layered structure with low interlayer binding energy (e.g. $ZrTe_5$ and $HfTe_5$). Some of them even show the topological behaviors. For example, Bernevig (2006) raised the prediction of energy of E1 and H1 bands versus mercury telluride (HgTe) quantum well thickness, in which the band inversion occurred at $d = 6.3$ nm, E1 turned from conduction band to valence band while H1 turned from valence band to conduction band (Figure 1-2). [6] One year later, the experimental proof was done by König (2007), HgTe quantum well structure has been proved as a 2D topological insulator and the critical thickness was exactly match with the prediction. [7]
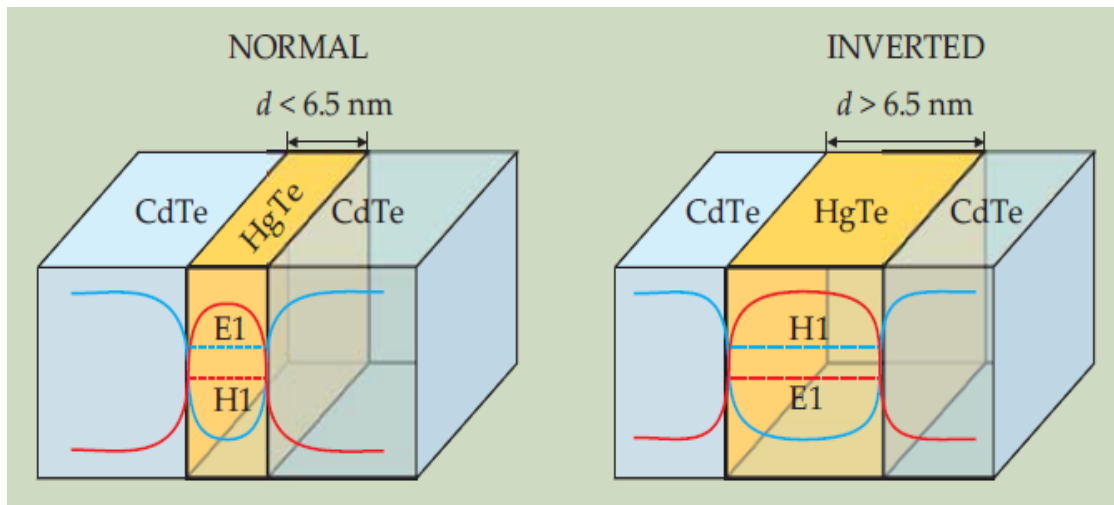
Figure 1-2 Band Inversion in HgTe Quantum Well Structure. [8]
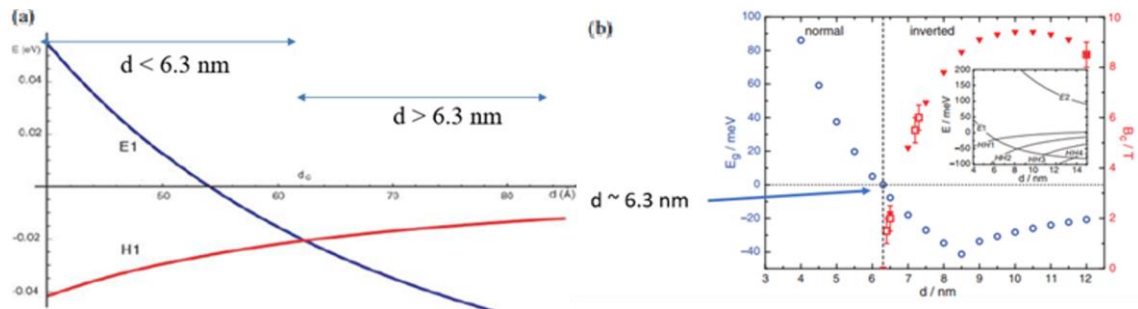
Figure 1-3 (a) Prediction of energy of E1 (blue) and H1 (red) bands versus HgTe quantum well thickness. [6] (b) Experimental energy gap versus HgTe quantum well thickness. [7]

Meanwhile, some other transition metal ditellurides (e.g. $HfTe_2$, $MoTe_2$ & WTe_2) have been studied. $HfTe_2$ thin film has been grown by MBE on AlN (0001) substrate and proved to be topological Dirac semimetals. [9] $MoTe_2$ and WTe_2 have been proved as topological Weyl semimetals in 2016, respectively. [10, 11]

According to Weng (2014), single layer $ZrTe_5$ and $HfTe_5$ have been predicted to be Large-Gap Quantum Spin Hall Insulators. [12] However, the prediction of single layer $HfTe_5$ still needs to be experimentally confirmed. Recently, the quantized transport properties of bulk $ZrTe_5$ crystal was reported by Wei Wang et al. (2018), that Shubnikov-de Hass (SdH) oscillations accompanied by quantized Hall resistance are not originated

from the surface state, but from the bulk state. They also suggested that each single layer ZrTe$_5$ should be considered as an independent 2D electron system while the bulk state of samples exhibits a multilayered quantum Hall effect. [13]

Besides the SdH oscillations observed in the bulk ZrTe$_5$, the large thermal power with Seebeck coefficient, $\alpha \approx \pm 80\ \mu V/K$; and the comparably low calculated interlayer binding energy (see Figure 1-4a), $E_b = 12.5\ meV/Å^2$, makes the ZrTe$_5$ a promising thermoelectric material. [12] The phenomenon of resistivity anomaly was also observed in the bulk ZrTe$_5$ with $T_p = 145\ K$, and this phenomenon can be further enhanced by external magnetic field. (see Figure 1-4) [14]
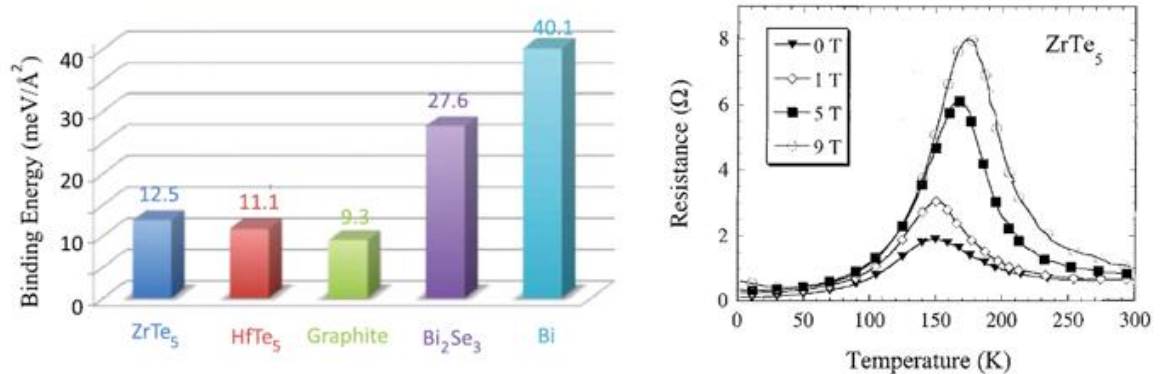
Figure 1-4 (a) Calculated interlayer binding energy for some layered compounds. [12] (b) R-T measurement of a single crystal ZrTe$_5$ for various applied magnetic field. [14]

Other zirconium tellurides also show various extraordinary properties, for example, superconductivity has been observed in bulk ZrTe$_3$ with $T_c < 2K$ exhibiting an increase in critical temperature up to 4.5 K by selenium doping. (see Figure 1-5) [15]
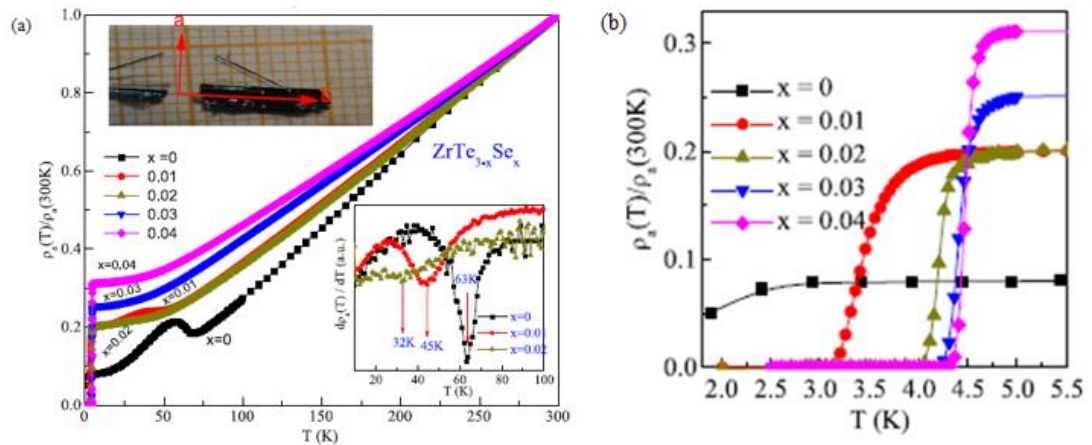
Figure 1-5 (a) Temperature dependence of normalized ρ_a for ZrTe$_{3-x}$Se$_x$. (b) Low temperature ρ_a. [15]

Previously, most of the researchers focused on bulk topological materials. Even some of them were working on the low-dimensional materials, they usually used the method of mechanical exfoliation. Physical or chemical deposition of topological thin films is rare, this motivates us to synthesize the transition metal telluride thin films and observe the non-trivial phenomena in the thin films.

Recently, Tsipas (2018) reported the growth of single and few-layered 2D semimetal ZrTe$_2$ by molecular beam epitaxy (MBE) on InAs(111) / Si(111) substrates. [16] The angle resolved photoelectron spectroscopy (ARPES) was used to study the electronic band structure of ZrTe$_2$ thin film. Dirac-like cone in 2-dimensions caused by the linear dispersion in ARPES along directions in k-space was observed at the zone center, indicating the massless 3D Dirac fermions. This also suggests that monolayer ZrTe$_2$ could be considered as the electronic analogue of graphene. (see Figure 1-6) [16]
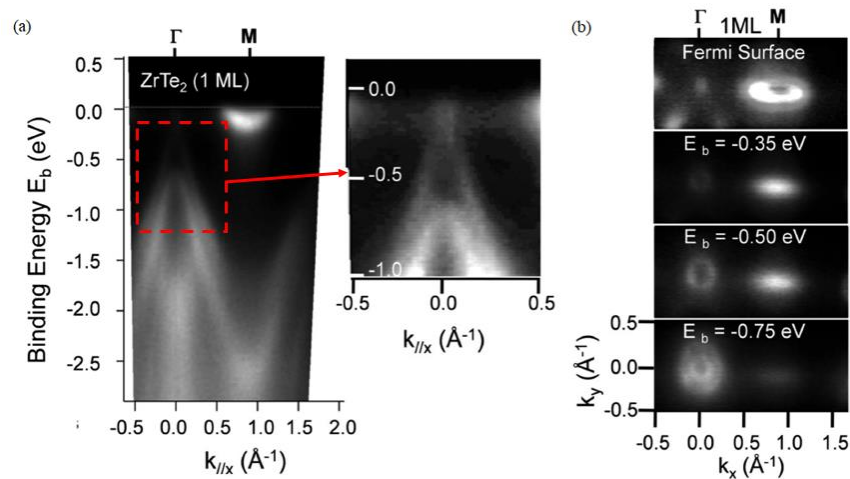
Figure 1-6 (a) Monolayer ZrTe$_2$ along high-symmetry crystallographic directions of the First Brillouin Zone using the HeI resonance line. (b) ARPES k$_x$−k$_y$ constant energy contours maps for the Fermi Surface and for different binding energies E$_b$ for 3 and 1 ML ZrTe$_2$. [16]

Tsipas (2018) studied the ZrTe$_2$ monolayer and few-layered thin film grown by MBE and suggested that the experimental result of the electronic band structure of monolayer and few-layered ZrTe$_2$ are both agree with the theoretical Density functional theory (DFT) calculations. However, the lack of electrical transport properties measurements still triggers the research interests.

Thus, in this project, I aim at the synthesis, structural characterization and the study of electrical transport properties of PLD grown transition metal tellurides thin films, especially zirconium tellurides.

1.2 Background of topological state

In classical physics, the electronic states of materials are simply classified as conductor and insulator. The discovery of semiconductor raised the concepts of energy band structure and carriers other than electrons, follow up by the magnets and more exotic phases such as the superconductor. Recently, a new class of electronic phase materials called "topological insulators" has been brought out, which exhibiting conducting surface or edge state and insulating bulk state. Interestingly, the surface state of topological insulators is considered as protected by the time reversal symmetry which means they cannot be destroy by impurities or imperfections.

Traditional insulators have an energy band gap separating the conduction and valence bands as shown in Figure 1-7a. When the materials against a strong spin-orbit coupling (SOC), the bands will mix together, leading to the so-called band inversion (see Figure 1-7b, c). The locations of the minimum point of conduction band and the maximum point of valence band in the typical band structure diagram of topological insulator (see Figure 1-7c) indicate the band inversion in topological insulator.
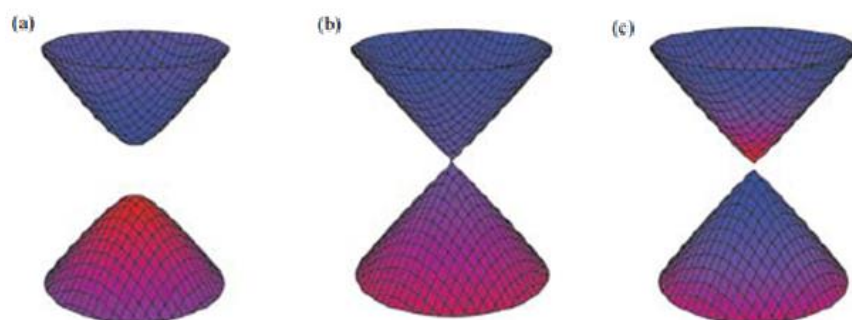
Figure 1-7 Band structure diagram of (a) Traditional insulator; (b) Bands mixing; (c) After band inversion [6]

1.2.1 Hall Effect

In 1879, Edwin H. Hall discovered the Hall effect, which plays an important role in the development of theoretical studies on topological insulators including the effect of external magnetic field on the electric current inside a metallic material. Unexpectedly, the experiment showed that a poled edge was induced in the metallic material when the external magnetic field is perpendicular to the electric current, and this phenomenon was suggested as a result of the Lorentz force. [17]
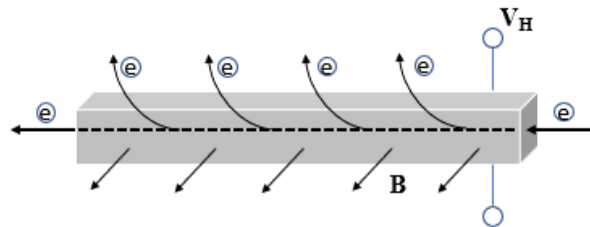
Figure 1-8 Set up of Hall Effect experiment.

In the Hall experiment, an external electric field and magnetic field **B** are applied to the metallic material while they are perpendicular to each other, as illustrated in Figure 1-78. When the charge carriers go through the metallic material, say electrons, will experience Lorentz force, F_B, resulting in deflection to the top side of the material. The direction of deflection can be determined using Right-Hand Rule.

As the electrons deflect and accumulate at the top side of the material, an internal E-field, **E** is induced, which is perpendicular to both external E-field and B-field. The Lorentz force, F_B can be calculated by:

$$\overrightarrow{F_B} = q(\vec{E} + v \times \vec{B})$$

where q and v are the charge and velocity of the charge carriers, respectively.

In equilibrium, the Lorentz force acts on the charged particles is equal to zero. By $V_H = EW$ and $I = q\rho_e vW$, Hall resistivity (also called Hall coefficient), R_H can be calculated

by:

$$R_H = \frac{V_H}{I} = \frac{B}{q\rho_e}$$

This equation shows that, for single charge carrier system, the Hall coefficient is linearly proportional to the magnetic field.

1.2.2 Quantum Hall Effect (QH)

Nearly 100 years later, in 1980, von Klitzing observed an unusual result in his experiment studying the Hall effect in a 2-dimensional electron gas (2DEG) under a strong magnetic field and extremely low temperature environment. [18] The classical Hall effect suggested that the Hall coefficient should be linearly proportional to the external magnetic field. However, in this experiment, a zero longitudinal conductance and quantum plateau of the Hall conductance at $\frac{ie^2}{h}$ (where h is the Planck's constant, i is the filling factor which equals to 1, 2, …) was observed. (see Figure 1-9)
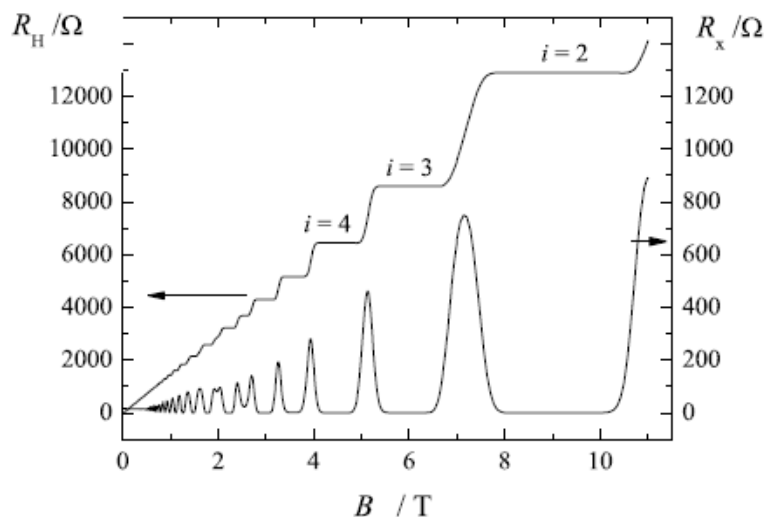
Figure 1-9 Typical Hall resistance plateaus in Quantum Hall Phase. [19]

In Figure 1-10, the electronic states of matter in quantum hall effect is shown. The charged

particle in a uniform magnetic field is undergoing a circular motion due to the Lorentz

force with radius of $r = \sqrt{(2n+1)\frac{h}{eB}}$. Interestingly, those particles nearby the boundary

of the material, will bounce back from the rigid boundary and skip forward along the

boundary but not escape from the material through the boundary. Thus, a one-dimensional

conductive channel was formed along the boundary, which is also called edge (or surface)

state. In addition, when a surface-state charged particle encounters an non-magnetic

impurity, it will simply take a detour and keeps going in the original path as there are no

backward-propagation mode for QH state, which also means, the quantum hall state does

not affect by the non-magnetic impurity. [8]
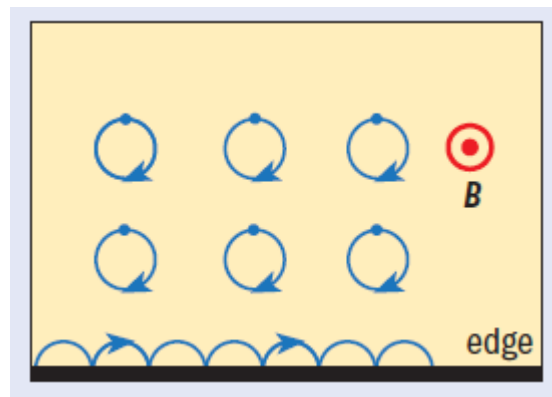
Figure 1-10 Electronic states of matter in Quantum Hall Effect. [20]

After all, the most significant feature of QH effect is that the charged particles in the bulk

of the materials are pinned or localized by the impurities or disorder, resulting in an

insulating bulk state which is the main characteristic of the topological insulator. [21]

Unfortunately, the QH effect is not applicable as it only takes place under strong external

magnetic field and extremely low temperature environment.

Thus, the Quantum Spin Hall (QSH) effect triggers lots of research interest in the

applicability of topological insulators because the similar electronic state can be achieved

in QSH without these two extreme environmental requirements.

1.2.3 Quantum Spin Hall Effect (QSH)

Unlike the quantum Hall effect, the topological state can also be achieved without strong magnetic field environment, in which the role of strong magnetic field was replaced by the spin-orbit coupling (SOC). The SOC effect is due to the interaction of an electron's intrinsic angular momentum, or spin, with the orbital motion of the electrons. This approach was first theoretically suggested that the QSH insulator can be made of two copies of QH system with opposite spins and Chern number. [22] However, scientists later concluded that the SOC in graphene is not strong enough to achieve the band inversion, which means the topological surface state cannot be achieved as the SOC in graphene is not strong enough. As the electrons move at relativistic speed, the strong SOC effect can usually be found in heavier elements. In 2007, the first QSH effect was observed in CdTe / HgTe / CdTe quantum well structure.[7]

Although similar electronic state and properties can be found in both QH and QSH state (conductive surface state, insulating bulk state and resultant carrier propagation unaffected by non-magnetic impurities), the mechanism of carrier propagation between them are completely different.

Be aware that, the edge state carriers in QH state can only propagate in opposite directions at different edges, meaning that only single path propagation is allowed. This results in the edge state carriers simply detour and keep propagate straightly when encountering non-magnetic impurities.

In contrast, the edge state carriers in QSH state can travel in four possible propagation modes: (Spin-up or Spin-down) and (Forward or Backward). (see Figure 1-11)
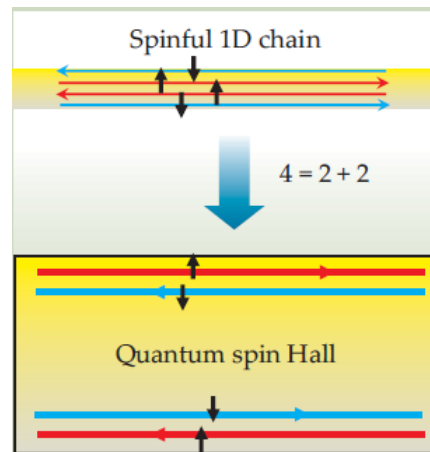
Figure 1-11 Electronic states of matter in Quantum Spin Hall Effect. [8]

Although there are both forward and backward movers at both top and bottom edges, the backscattering of electrons against non-magnetic impurities is forbidden.

For better understanding, we can take the property of interference in light wave as an example.
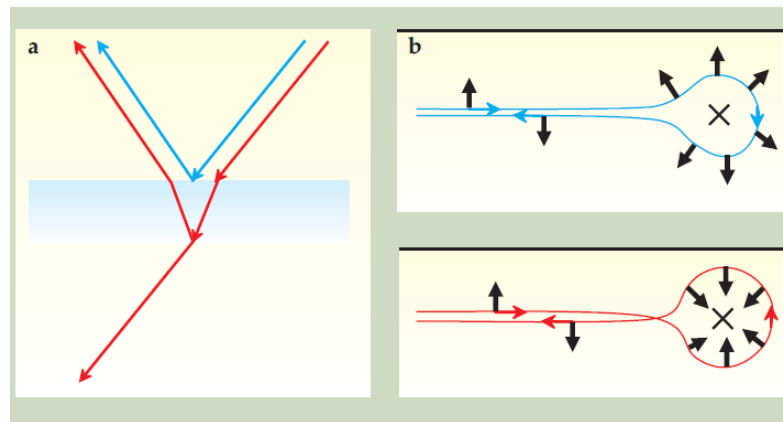
Figure 1-12 (a) Interference of reflected light waves from different faces of a lens. (b) Two possible paths of backscattering electrons against non-magnetic impurities. [8]

In many optical instruments, such as camera lenses and eyeglasses, an anti-reflection coating is used to prevent the reflected light by making its interference becomes destructive. As the reflected light from second surface obtains a phase change of π, the path difference of reflected light from first and second surfaces is equal to π, meaning

that the interference of these two reflected lights is destructive to each other.

Refer to the situation of electrons backscattering by non-magnetic impurities, electron propagation also has the property of interference as photon. When related to Time Reversal Symmetry (TRS), the backscattering electrons are differed by a full $\pi-(-\pi) = 2\pi$, rotation. According to the principle of quantum mechanics, the wavefunction of a spin - 1/2 particle obtains a negative sign upon a full 2π rotation.

CHAPTER 2 METHODOLOGY

In this chapter, experimental methods from thin film growth to structural characterization and electrical transport characterization are introduced.

2.1 Pulsed-laser deposition (PLD)
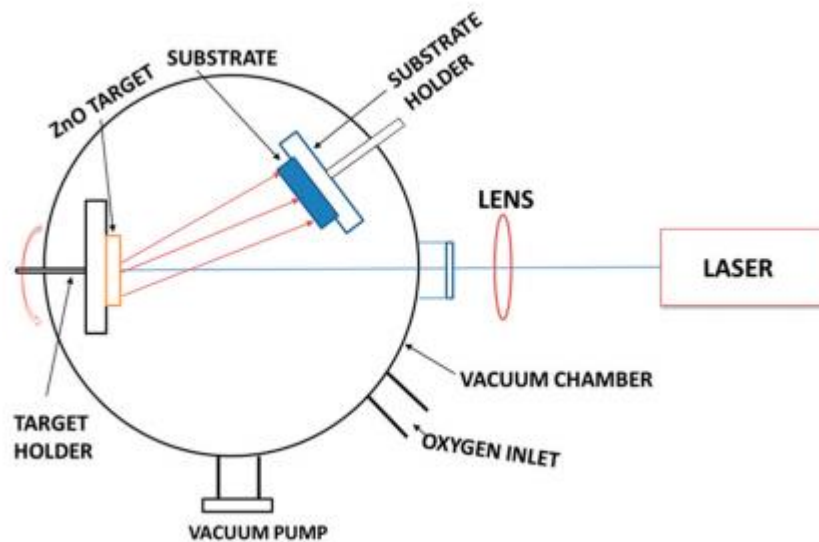
Figure 2-1 Typical setup of PLD Experiment. [23]

Figure 2-1 shows the typical setup of PLD system used in this project. Basically, the laser beam is focused on the PLD target by an optical lens through a highly transmitted window of the PLD chamber. The PLD chamber is pumped by a vacuum system to achieve a very high vacuum level (typically $< 7\times10^{-5}$ Pa) for thin film deposition. The substrate holder and the target holder are connected to a rotation system which greatly increase the uniformity of the thin films. The substrate holder is also connected to a heater and thermocouple for monitoring the heating process of the deposition. The following shows the detailed processes of thin film deposition in this project:

1.   Substrates are attached on the substrate holder of the PLD system by silver paste.

2.   Substrate holder is put inside the PLD chamber and covered by a shutter while

laser is executed to clear up the impurities on the PLD targets.

3.   Remove the shutter and heat up the substrate holder to the desired temperature.

4.   Focus the laser beam on the Zr-Te target after the vacuum level reach to the base pressure ($\sim$5.0 x 10^{-5} Pa).

5.   After the deposition of thin film, cool down the substrate holder naturally inside the chamber until it reaches to the desired substrate temperature (200 or 250 ℃) for capping layer deposition.

Advantages and Disadvantages

Laser ablation for thin film growth has a number of advantages compared to other thin film deposition methods:

i.   Almost any condensed matter materials can be ablated due to the wide range of laser power and unlimited laser energy density by adjusting the convex lens.

ii.   Relatively low deposition temperatures are required because of the high kinetic energy of the ablation plume species.

iii. High reproducibility and high deposition rate.

However, PLD also has some technical disadvantages:

i.   Impurities in the target materials may contaminate the thin film, thus, high purity target and gasses are required to avoid the contamination.

ii.   High energy density leads to difficulties in synthesizing mono-layer thin film and large area continuous thin film.

iii. High kinetic energy sometimes leads to crystallographic defects in thin film.

Stages and mechanism of the PLD processes
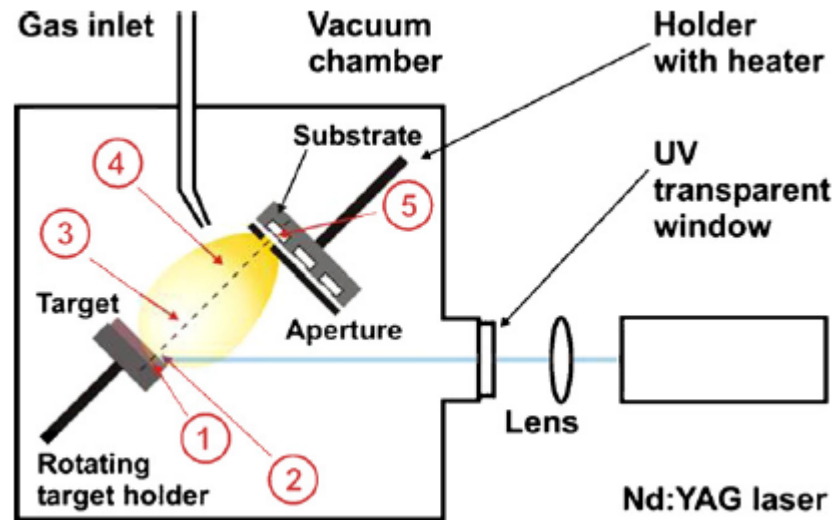
Figure 2-2. Overview of the stages of PLD. [24]

Figure 2-2 shows the overview of different stages of PLD process which can be described by five stages:

1.   Light interactions with target

2.   One-dimensional plume expansion

3.   "Free" three-dimensional plume expansion into vacuum

4.   Plume interactions with background gas

5.   Thin film growth

For a typical PLD experiment, the laser is focused on the target by an optical lens, then a one-dimensional ablation plume is formed by absorbing the laser energy through direct photo excitation. During stage 3, a three-dimensional plume is formed by further absorbing the laser energy for atoms and ions inside the one-dimensional plume. [25-28] After that, if the experiment is conducted under a background gas environment, the three-dimensional plume will go through stage 4. At this stage, the plume is slowed down by interactions with the background gas and then mix up with the background gas molecules,

eventually diffuse out of the confinement. [29-32] Finally, depending on the arrival energy of the plume atoms, the collected plume atoms will grow as a thin film on the substrates in different growth modes. [33]

Light Interactions with Target

For a typical laser used in PLD with wavelength 248 nm, the energy of laser is absorbed by the electrons of the target materials through band electron transition in the form of photons. So, the refractive index of different target materials will greatly affect the ablation yield of atoms. Typically, the ablation yield of the refractory metals (e.g W, Mo, Ta) and volatile metals (e.g Bi, Sn, In) are 0.1 x 10^{15} atoms/pulse and 10 x 10^{15} atoms/pulse, respectively, with laser energy density equals 2 J/cm^2. (see Figure 2-3)
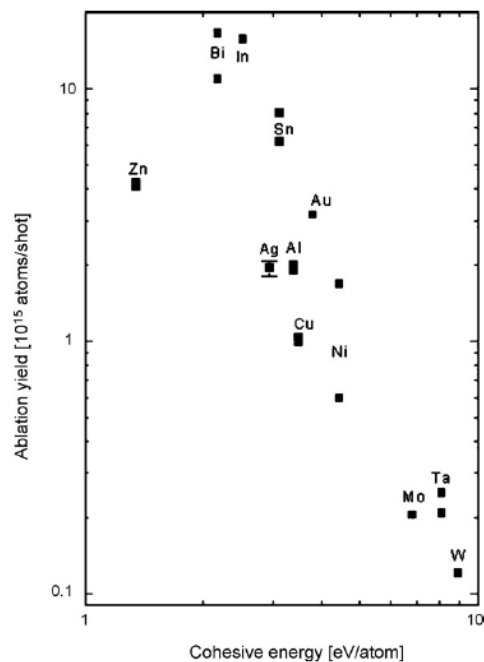
Figure 2-3. The dependence of laser ablation yield on the volatility of different materials.

[34]

However, due to the mechanism of EM wave penetration, the absorption of laser energy by the ablation target is limited by a parameter called penetration depth which depends

on the absorption coefficient, α, of the ablation target. The penetration depth of the target can be calculated using the equation $L_p = \frac{1}{\alpha}$. In the meantime, the heat diffusion length which heating energy travels inside the ceramic target can be calculated using the equation $L_p = \sqrt{D_{th}\tau}$, where D_{th} is the thermal diffusivity and τ is the pulse duration. Be aware that the plume expansion should take place at the surface of the target, it implies that the case of $L_d \ll L_p$ is the preferred one.

One-Dimensional Plume Expansion

In stage 2, the one-dimensional plume is formed by absorbing electromagnetic energy from the laser beam forming all possible ions. However, since the plume continues to absorb laser energy, the energetic electrons in the plume will produce a plasma with ions, and thus, the plume expansion resulting in the creation of plasma so-called Kundsen Layer. [35] The Kundsen Layer has a typical thickness of 30-100 μm with pressure of 5-10 bar. [24]

"Free" Three-Dimensional Plume Expansion

In stage 3, the plume plasma expands parallel to the normal vector of the target surface towards the substrate due to the coulomb repulsion between electrons and the pressure gradients in the initial plume [27, 36, 37]. According to the adiabatic expansion model, which is introduced by Singh and Narayan [38], the plume expands adiabatically in vacuum and finally perform free motion of plume particles.

Plume Interactions with Background Gas

Different from the case of deposition in high vacuum environment, the atoms inside the plume diffuse out and mix up with the background gas molecules rather than propagating toward the substrate in constant velocity. Then, the target atoms migrate to the substrate

or the chamber walls and start to diffuse and nucleate on the substrate, and thus, thin films are formed on the substrates. [29-32] Besides, the mass of atoms in plume is important for the propagation dynamic, for instance, the stopping length for the plume has been derived by Strikovski and Miller. They proved that heavy ion plume will have a larger stopping distance. [39] The angular distribution of the plume atoms also shows the dependence of the mass of atoms that the broadening of the angular distribution of heavy atoms occur at a much lower pressure than that of light gases, meaning that light atoms in a heavy gas are scattered much more than heavy atoms in a heavy gas. [30, 33, 40] (see Figure 2-4)
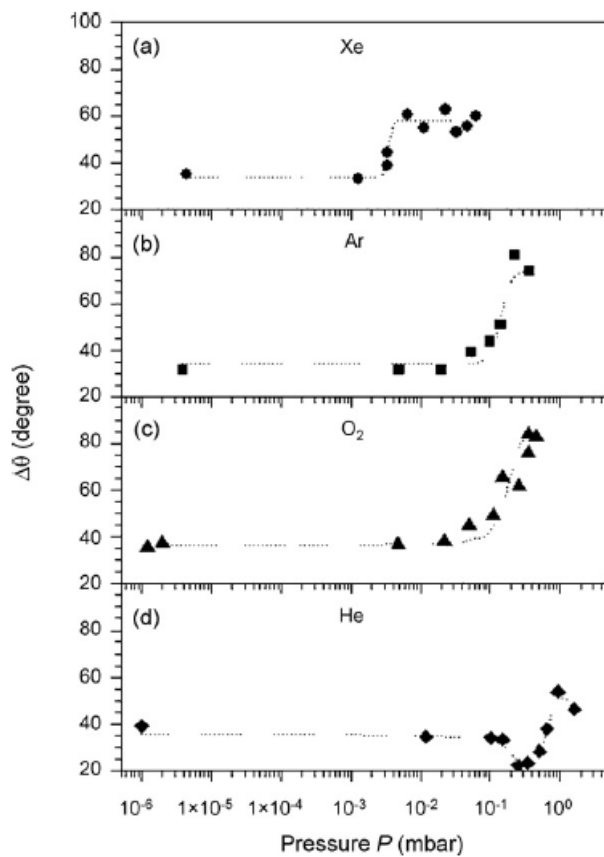
Figure 2-4. Full-width-half-maximum $\Delta\theta$ of the angular distribution for Ag-atoms in different background gases versus pressure. [41]

Thin Film Growth on Substrate

The growth process of thin film in micro-scale is a very complicated process and it has been well studied. [42] Due to the high kinetic energy of the arrival atoms, atoms usually diffuse along the substrate surface for some distance, rather than stick on the original position that it arrives on. (see Figure 2-5)   When stabilized stabilization   on substrate, the nucleation of atoms will start due to the energetically favorable situation provided by the substrate temperature, i.e., finally the growth of thin film will take place.
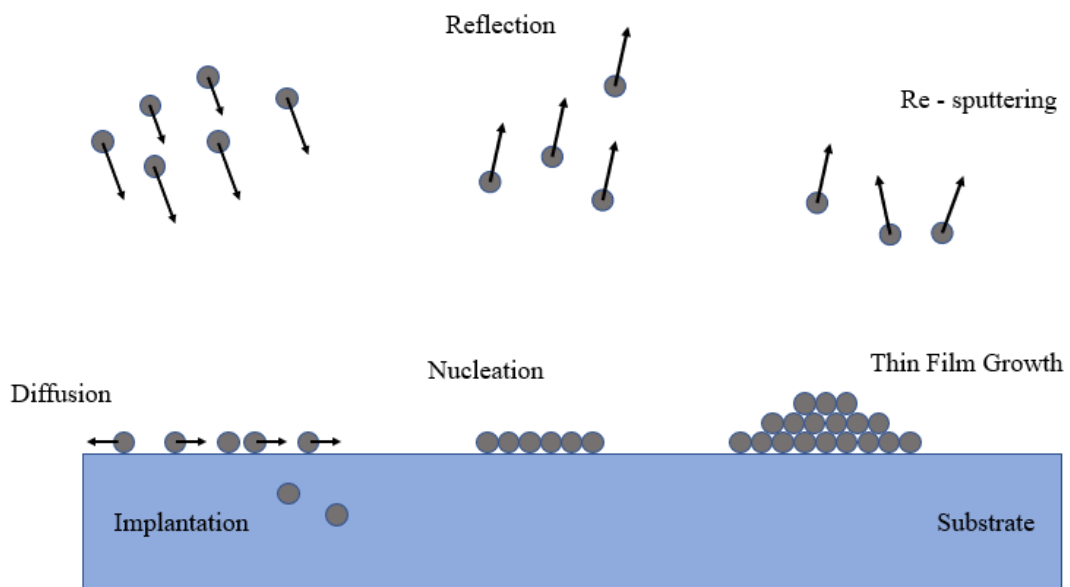
Figure 2-5. Nucleation process of atoms on substrate in PLD.

Figure 2-5 shows that there are some non-preferred processes of the arrival atoms in PLD: (1) atom reflection from the surface, (2) re-sputtering of surface atoms by the ablation atoms, and (3) implantation of ablation atoms. The reflection of atoms from the surface only affects the efficient of the deposition but has no effect on the quality of the grown thin film. In contrast, the re-sputtering of surface atoms by the ablation atoms is an issue that may affect the thin film quality. For example, an experiment depositing a metallic thin film using PLD showed that there is a re-sputtering of thin film atoms during the

experiment in an ambient gas. [43] In this experiment, a re-sputtering rate of 0.55 for silver atoms at energy density of 4.5 J/cm^2 has been measured, indicating that only half of the arriving Ag atoms are finally remained on the substrate as a thin film. Implantation of ablated ion has been observed in PLD experiment for a few times. [44-46] In general, the ablated atoms with high mass has lower implantation range because of the high nuclear stopping force.

Besides the non-preferred processes of the arrival atoms in PLD, different growth modes of thin films are of a more complicated topic. The word "epitaxy" is used to describe the growth of a high-quality single crystal thin film on a single crystal substrate with a fixed orientation. There are two types of epitaxy growth, one is homo-epitaxy and the other one is hetero-epitaxy. Homo-epitaxy means that the thin film and the substrate are of same materials, while hetero-epitaxy denotes that the thin film and the substrate are of different materials. However, the crystallographic relationship between thin film and substrate can be greatly affected by the difference in the lattice constants between them. This can be descried by a parameter called lattice mismatch which can be calculated by:

$$m = \frac{a_{film} - a_{substrate}}{a_{substrate}} \times 100\%$$

The growth mode of thin films in the early stages depend on the sign (+ or -) of lattice mismatching. In general, there are four epitaxy growth modes in different cases of lattice mismatch. (see Figure 2-6)
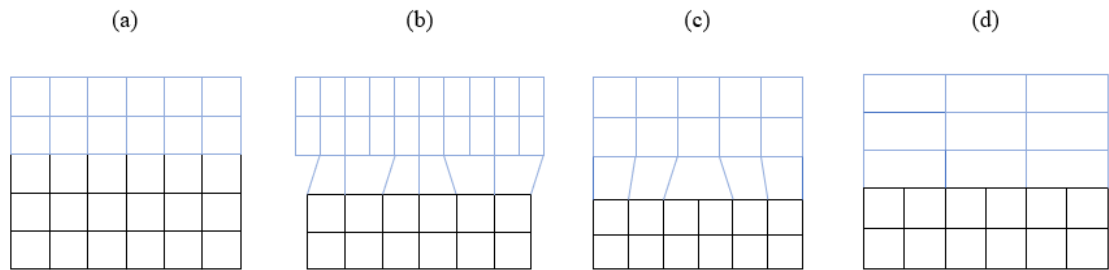
Figure 2-6. Different epitaxy growth modes. (a) Homo-epitaxy (b) tensile hetero-epitaxy (c) compressive hetero-epitaxy (d) domain hetero-epitaxy

Figure 2-6(a) shows the schematic diagram of homo-epitaxy growth of thin films on the substrate. Generally, this growth mode takes place when the lattice mismatch m is less than 7%. For cases when the lattice mismatch is larger than 7% with negative sign, which means $a_{film} < a_{substrate}$, the lack of bonding between thin film atoms and substrate atoms result in the tensile stress inside the thin film as shown in Figure 2-6(b). In contrast, for the cases when the lattice mismatching is larger than 7% with positive sign, which means $a_{film} > a_{substrate}$, the lack of bonding between thin film atoms and substrate atoms result in the compressive stress inside the thin film as shown in Figure 2-6(c). However, if the lattice mismatch is equal to a certain value that satisfy the domain hetero-epitaxy (see Figure 2-6(d)), the bonding between thin films and substrate is relatively stronger than that of other hetero-epitaxial growths.

Due to the big influence of lattice mismatch in the epitaxy growth modes, this factor has long been realized as a bigobstacles for heterostructure grown on substrates with large lattice mismatch between materials. However, it was found that good heterostructures can be grown even between materials having large lattice mismatch with van der Waals epitaxy. [47-49] (see Figure 2-7)
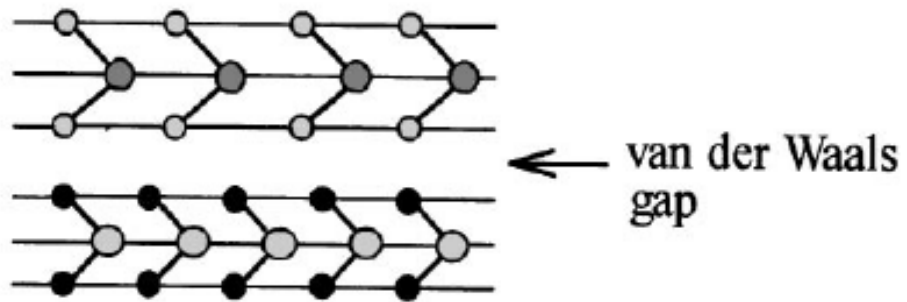
Figure 2-7. Interfaces connected by van der Waals gap. [50]

2.2 X - ray diffraction (XRD)

XRD is a non-destructive structural characterization technique which can be used for investigating the crystallinity and growth orientation of thin films. Using XRD, lattice parameters, crystallographic information of thin film samples and even the crystallographic relationship between thin film and substrates can be completely determined. In this project, Rigaku SmartLab 9kW is used for XRD characterization.

Theta - 2Theta Scan

In crystallography, a term called Miller indices (hkl) is used to index the crystallographic planes of crystal structure. In X-ray diffraction, the incident angle leading to the maximum diffraction can be calculated using Bragg's Law:

$$2d_{hkl}sin\theta = n\lambda$$

where d_{hkl} is the interlayer spacing related to the (hkl) plane of the crystal, θ is the incident angle of the X-ray, λ is the wavelength of the X-ray. The schematic diagram of Bragg's Law is shown in Figure 2-8.
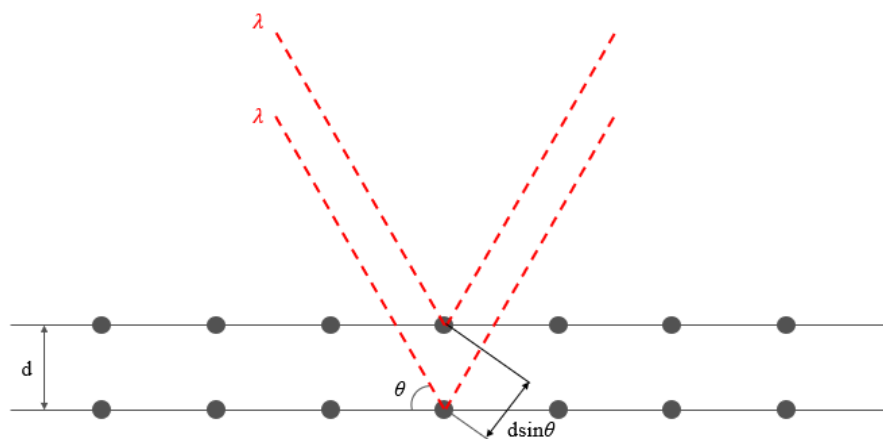
Figure 2-8. Schematic diagram of Bragg's Law.

Phi Scan

Different from the $\theta - 2\theta$ scanning mode, Phi scan can be used to investigate and determine the in-plane epitaxial relations in highly oriented thin films. Apart from the rotational angle of the detector with respect to the incident beam in $\theta - 2\theta$ scanning mode, 2θ, the phi scan investigates the in-plane information also using χ - axis and $\emptyset$ - axis.
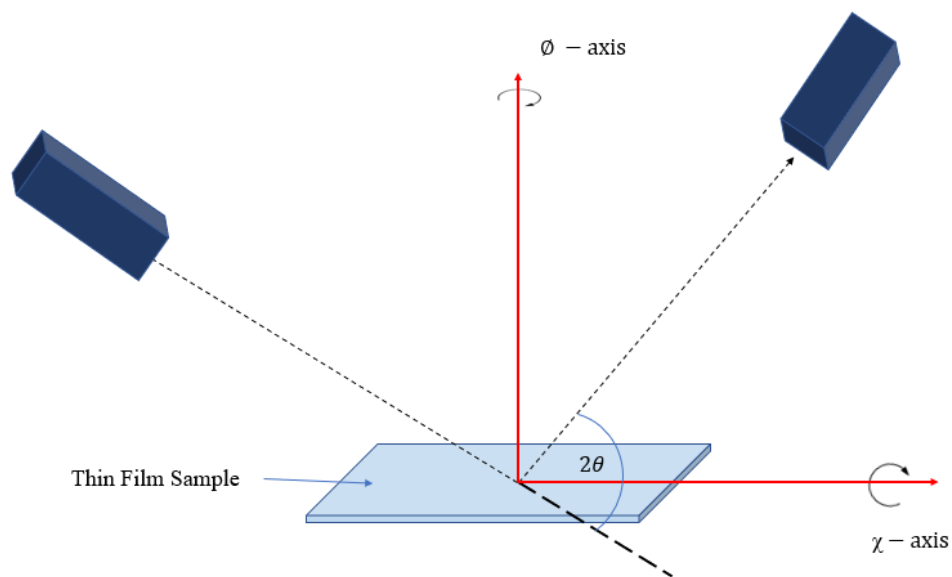
Figure 2-9. Schematic diagram of the Rigaku SmartLab diffractometer with rotation along χ - axis and $\emptyset$ - axis under phi scanning mode.

The phi scan is an advanced scanning mode beyond the $\theta - 2\theta$ scanning mode. Take a thin film sample with hexagonal structure as an example, before the confirmation of the hexagonal crystal structure, if the result given by the $\theta - 2\theta$ scanning mode shows certain peaks indicating the (0001) and (0002) planes of the preferred hexagonal structure, it is too rash to say that the unknown sample has a hexagonal crystal structure because it might be a cubic crystal structure but with similar d-spacing in (0001) and (0002) planes. However, from the crystallography, we know that the hexagonal crystal structure has six

equivalent $(10\bar{1}2)$ planes along $\emptyset$ - axis rather than four for cubic structure, the hexagonal crystal structure of an unknown sample can be confirmed using phi scan.

The procedures of phi scan are shown below:

1.   Determine the out of plane orientation of the thin film, for example (0001).

2.   Calculate the intersection angle (χ) of (0001) and $(10\bar{1}2)$ of the thin film (It depends on the lattice parameter of the material.)

3.   Set the calculated χ value and start a $\theta - 2\theta$ scan to obtain an accurate 2θ value where the maximum diffraction intensity of $(10\bar{1}2)$ plane appears.

4.   Set the calculated χ values and the measured 2θ values and start the Phi scan from 0º to 360º.

2.3 Transmission electron microscopy (TEM)

In this project, a Jeol JEM-2100F Scanning Transmission Electron Microscopy (STEM) is used to investigate the structural information of thin film samples. Figure 2-10 shows the interaction of electron beam with TEM specimen.

Operation Modes
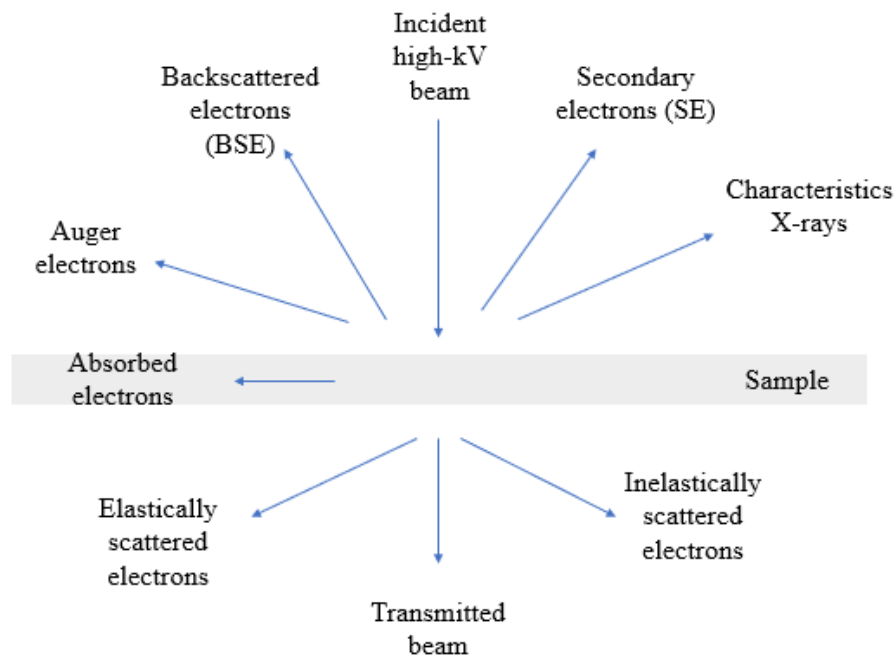
Figure 2-10. Interaction of electron beam with specimen.

The characteristics X-rays can be used for elemental analysis which called energy dispersive X-ray (EDX) analysis; it can also be used to estimate the relative abundance of difference element in the specimen. However, as the mechanism of EDX is to match the wavelength of emitted characteristics X-rays from the specimen to the characteristics X-rays database, the overlapping wavelength of X-ray of different elements will affect the accuracy and reliability of the EDX result.

The inelastically scattered electrons can be used for electron energy loss spectroscopy (EELS), they are produced as the energy loss of electron via inelastic scattering of electrons with specimen, and the lost energy is measured using an electron spectrometer. Under the scanning dark field mode of the STEM, the electron beam is focused to a fine spot, so the EELS can be used for element mapping at atomic resolution.

Sample Preparation using Focused Ion Beam (FIB)

The transmission of unscattered incident electrons is inversely proportional to the thickness of TEM specimen, meaning that the decrease of the specimen thickness promotes the transmission of electrons, so the resolution will be greatly enhanced because of the reduced chromatic aberration effects for thick TEM specimen. The typical thickness of TEM specimen is less than 100 nm. To obtain a thin enough cross-sectional TEM specimen, FIB (Jeol JIB-4500) is used in this project.
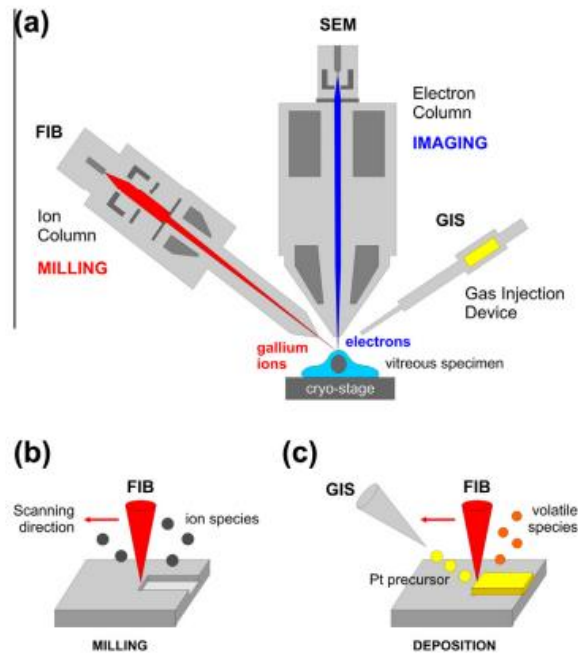
Figure 2-11. (a) Schematic diagram of FIB/SEM Set Up (b) Ion beam milling mode (c) Ion beam-assisted deposition [51]

FIB instrument is usually connected to a scanning electron microscope for monitoring the

milling process in a non-destructive way for imaging. Gallium ions are accelerated and focused to the specimen surface inside FIB, the kinetic energy of the Ga^+ ions is transferred to the samples through multiple ion-atom collisions, as a result, surface atoms overcome their surface binding energy and be sputtered out. Besides, the ion-beam-assisted deposition mode is usually used to deposit a Pt layer on the specimen surface before ion etching. The Pt layer acts as a protective layer because the Ga^+ ions may completely damage the specimen of thin film samples.

The detailed processes of FIB are shown below:

1. Select a clean region on the specimen.

2. Deposit Pt layer on the selected region using the ion-beam-assisted deposition mode.

3. Mill the upper and lower regions of the selected region covered by Pt layer with large ion beam current density along vertical axis of specimen (red dotted line in Figure 2-12).

4. Repeat step 3 with decreased beam energy along rotated direction (green dotted line in Figure 2-12) until the bottom of the target region is only connected with the specimen by a thin region.

5. Cut the bottom thin region below the target region (see Figure 2-12).
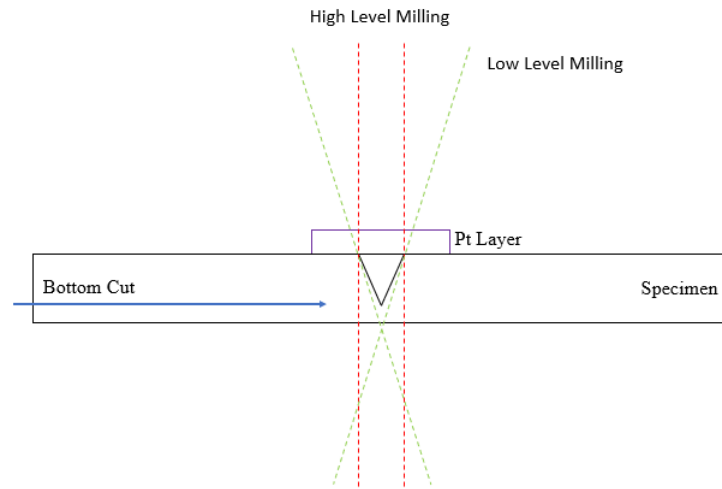
Figure 2-12. Schematic diagram of FIB processes.

Sample Preparation Using Grinding and Ion Milling

Although using FIB for TEM sample preparation is convenient, its disadvantage in high cost and limitation in preparing TEM plane-view specimen make the mechanical grinding method an alternative way for sample preparation.

Thin Film cross-sectional (Steps 3-5 only for Plane-view) sample preparation procedures:

1.   Stick the sample with a same but clean substrate face-to-face using suitable amount of M-bond (see Figure 2-13).
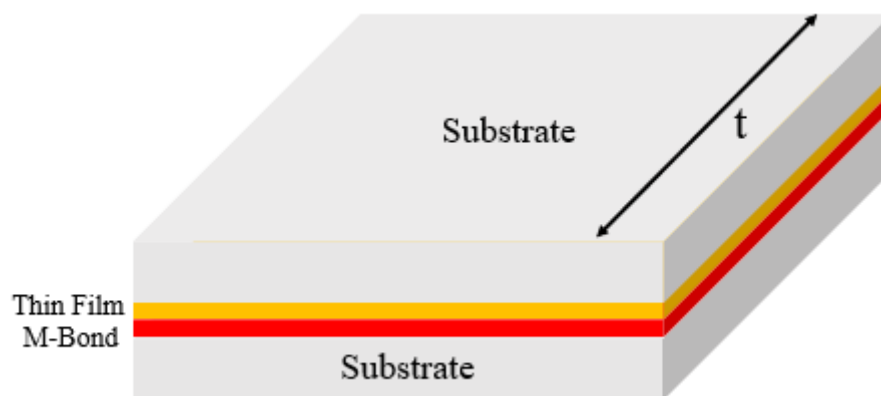
Figure 2-13. Schematic diagram of cross-sectional TEM sample.

2.   Stick the sample on the grinding tool using wax and start grinding sample until one

of the sides is uniform enough and been well-polished.

3. Stick the well-polished side (thin film side for plane-view) of sample on a hollow copper grid using M-bond.

4. Stick the sample on the grinding tool using wax and grind the specimen mechanically using sand paper and diamond abrasive until $t < 20\mu m$, and then polish it with polishing paper.

5. Use ion milling (Model number: Gatan 691) for further thinning the specimen, argon ions are commonly used in ion milling, they are accelerated by 3~6 kV DC voltage for milling out the atom in specimen. The schematic Diagram of ion milling is shown in Figure 2-14.
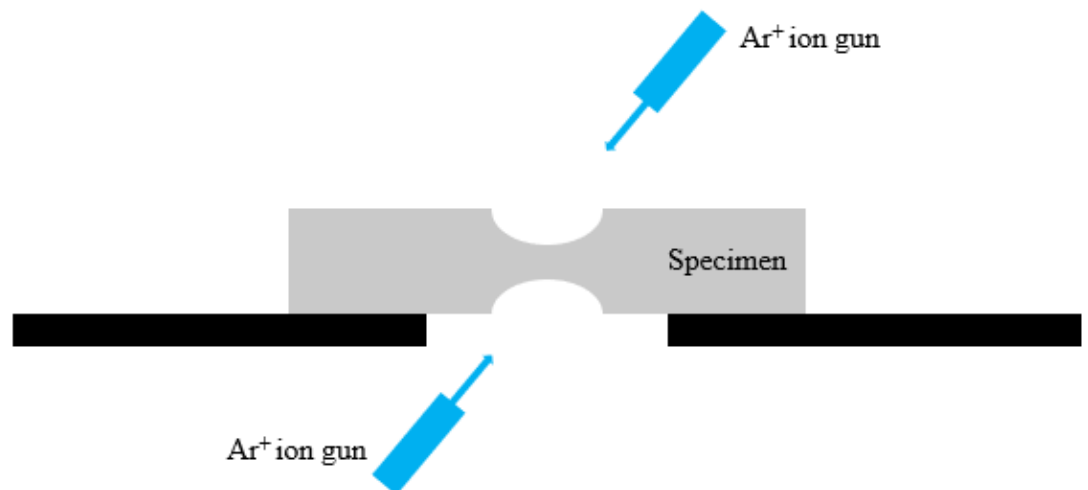
Figure 2-14. Schematic diagram of ion milling.

2.4 Physical property measurement system (PPMS)

The electrical, magnetic and thermal properties of various materials can be measured by the Quantum Design PPMS, which is constructed by Quantum Design Inc. The maximum capable magnetic field is 9 T with resolution of 0.2 mT at 9 T. The accessible temperature range is between 1.9 K to 400 K using ^{4}He. In this project, the Electro-Transport

measurement system was used to examine the electrical transport properties of thin film samples under extreme conditions.

Resistivity Measurement (R-T)

Four-probe method is used to measure the electrical transport properties of the thin film samples as shown in Figure 2-15.
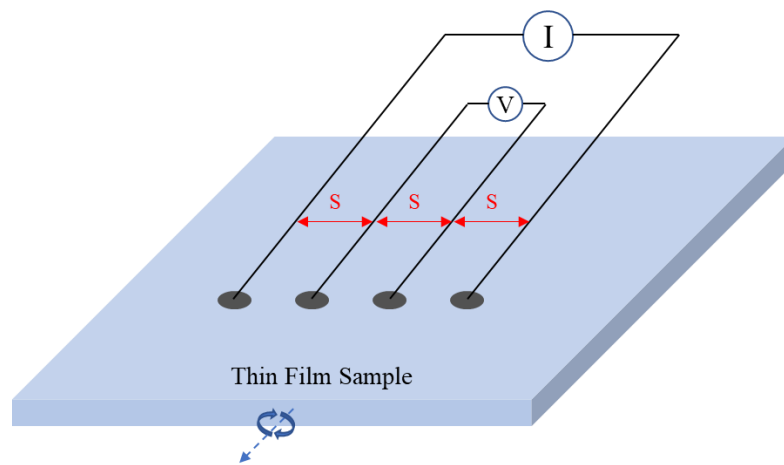
Figure 2-15 Schematic diagram of resistivity measurement using four-probe method with current source I, measured voltage V_{xx}.

In four-point probe method, a current source is connected to two outer probes, the resistivity can be obtained by measuring the voltage through the inner probes. Compared to the conventional two-point probe method, this method is more preferable because the contact and spreading resistances associated with the two-point probe are large, and the true resistivity cannot be separated from the measured resistivity. For thin film samples, the measured resistance is usually very low, meaning that the percentage of error in measured voltage is relatively high as the contribution of voltage drop in the contacts. Therefore, four-point probe method should be carried out. In four-point probe measurement, little contact and spreading resistance is associated with the voltage probes

and hence one can obtain an accurate calculation of the resistivity.

In this project, the magnetoresistance (MR) at various magnetic field (both perpendicular and parallel to the sample) was measured to investigate how the resistivity of thin film varies with the temperature and how this relationship is affected by various magnitude and direction of external magnetic field.

MR can be calculated as:

$$MR\ (\%) = \frac{R_B - R_0}{R_0} \times 100\%$$

Where R_B is the resistivity of sample under external B-field, R_0 is the resistivity of sample without external B-field.

Refer to the special transport properties in the topological state, negative magnetoresistance (NMR) and even quantum oscillation can be observed. Both quantum hall effect and quantum spin hall effect result in a great decrease in the resistance of surface state under a strong magnetic environment. Besides the NMR, giant magnetoresistance (GMR) also trigger lots of researches due to its useful applications such as spin-valves sensors. [53]

Hall Measurement
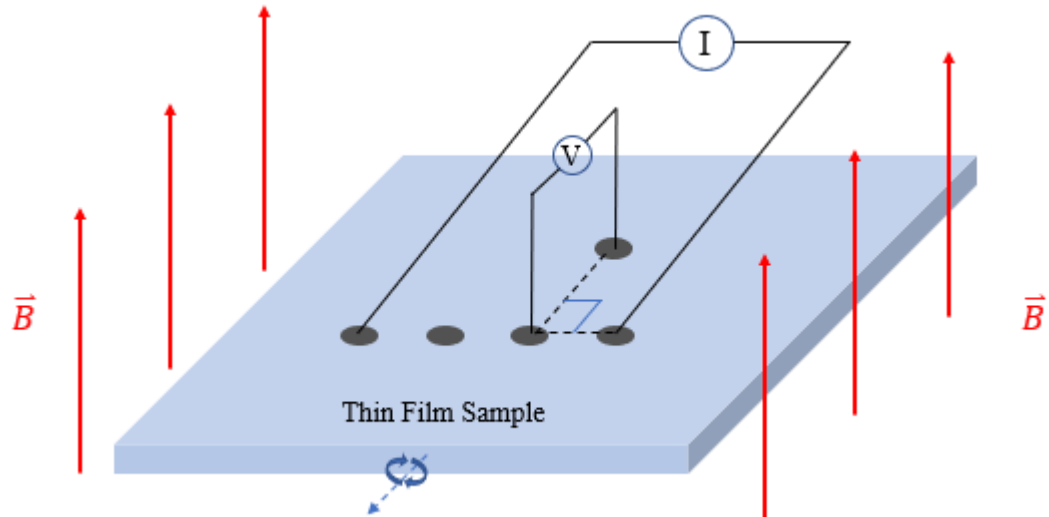
Figure 2-16 Schematic diagram of Hall measurement using four-point probe method with current Source I, external magnetic field $\vec{B}$ and measured voltage V_{xy}.

Different from the resistivity measurement, the measured voltage V_{xy}, also called the Hall voltage, is perpendicular to the direction of current flow. The direction of magnetic field is fixed in PPMS, so to investigate the change in resistance with different direction of B-field, the thin film samples can be rotated along y-axis to achieve a I // $\vec{B}$ situation. Refer back to 1.2.1, by $R_H = \frac{V_H}{I} = \frac{B}{q\rho_e}$, serval parameters of the sample can be measured using the Hall Measurement, such as Hall Voltage, Hall Coefficient, charge carrier density. The type of charge carriers (electrons or holes) can also be determined.

CHAPTER 3 PULSED-LASER DEPOSITION OF ZrTe₂ THIN FILMS ON SAPPHIRE (0001)

From the structural symmetry consideration, sapphire (0001) is the first choice as substrate since its hexagonal lattice on (0001) surface is the same as $ZrTe_2$ and $ZrTe$. Sapphire has hexagonal crystal structure with lattice constants $a = b = 4.785$ Å and $c = 12.991$ Å. Besides, the electrical insulating property of sapphire makes it convenient for electrical measurement of thin films grown on it.

The crystallographic data of different zirconium tellurides with different stoichiometric ratio is shown in Table 3-1, in which both $ZrTe$ and $ZrTe_2$ crystallized in hexagonal structure with similar lattice constants a and c.

Table 3-1. Crystallographic data of zirconium tellurides. [12, 54]

Compound	Crystal Structure	a (Å)	b (Å)	c (Å)
ZrTe	Hexagonal	3.95	\	6.660
ZrTe₂	Hexagonal	3.952	\	6.64
ZrTe₅	Orthorhombic	4.036	7.25	13.843
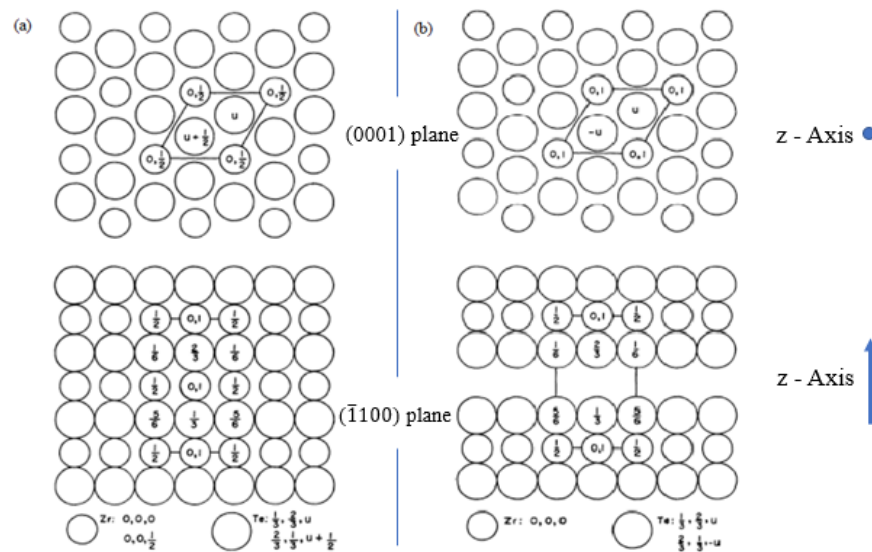
Figure 3-1. (0001) and ($\bar{1}$100) projection of (a) ZrTe and (b) ZrTe$_2$ [55]

Figure 3-1 illustrates the (0001) and ($\bar{1}$100) projection of ZrTe and ZrTe$_2$, in which the hexagonal crystal structures of them are almost the same except the difference in atomic distance along the [0001] direction.

One can see that, the main difference between ZrTe and ZrTe$_2$ is the lack of one-layer Zr atoms in a very similar structure. Consequently, if high-resolution TEM imaging is performed along a direction perpendicular to c-axis, the ZrTe$_2$ (0001) plane with lattice spacing equals 6.66 Å should easily be observed; while for ZrTe (0001), it may only show lattice spacing with half of this value. This difference should also be seen by electron diffraction and x-ray diffraction.

As the mechanism of XRD is to investigate the intensity of diffraction peak while the lattice atoms act as diffraction grating, the dominant XRD peak of ZrTe should be (0002), meaning that the intensity of ZrTe (0001) peak should be very low compared to the (0002) peak. However, the Zr-absent layer of ZrTe$_2$ contributing in the diffraction peak of ZrTe$_2$ (0001), which means even the lattice constants c of both ZrTe and ZrTe$_2$ are similar to

each other, we can determine the phase of our thin film by the existence of ZrTe (0001) peak in XRD.

The band structure of zirconium ditelluride ($ZrTe_2$) shows exotic characteristic of the crossing of valence and conduction bands along high symmetry lines. This may indicate topological 3D Dirac semimetal behavior. [16] The transport properties are studied by PPMS.

3.1 Thin Film synthesis experiment

Thin film samples are synthesized by Pulsed-Laser Deposition. The Coherent Excimer Laser used in this experiment is krypton fluoride laser with wavelength equal to 248 nm. Thin film samples are synthesized using various deposition conditions as shown in Table 3-2.

Table 3-2. PLD deposition condition of thin films on sapphire (0001).

Samples	(Zr-Te) growth Temperature (°C)	Laser Parameter on Zr-Te Target	(Al-N) growth Temperature (°C)	Laser Parameter on Al-N Target
1	450	5Hz, 10mins, 250mJ	250	5Hz, 30mins, 300mJ
2	500	5Hz, 10mins, 250mJ	250	5Hz, 30mins, 300mJ
3	550	5Hz, 10mins, 250mJ	250	5Hz, 30mins, 300mJ
4	580	5Hz, 10mins, 250mJ	250	5Hz, 30mins, 300mJ
5	600	5Hz, 10mins, 250mJ	200	5Hz, 30mins, 300mJ
6	650	5Hz, 10mins, 250mJ	250	5Hz, 30mins, 300mJ
7	700	5Hz, 10mins, 250mJ	250	5Hz, 30mins, 300mJ
8	750	5Hz, 10mins, 250mJ	250	5Hz, 30mins, 300mJ

A composite with Zr-Te (molar ratio = 1:5) is used as the PLD target for the $ZrTe_x$ thin film growth. The base pressure of deposition chamber is within 5.0×10^{-5} Pa to 5.5×10^{-5} Pa. After $ZrTe_x$ film deposition, AlN_x capping layer was applied to protect the telluride thin film from the moisture and oxygen in air because it was found that the synthesized thin film samples were extremely unstable under ambient atmosphere. It was observed that the resistance is nearly 10^6 times larger after exposing a capping layer free thin film sample in air for one hour. This instability leads to the difficulty in further study on both structural and electrical properties. Consistently, the result after applying AlN_x capping layer achieved the initial objective. With a capping layer, the degradation rate of thin film greatly reduced; the thin film resistance measured by multi-meter shows nearly no change after exposed in air for few days. The stability can be months if stored in vacuum with pressure lower than 2 Pa.

The deposition temperature for AlN capping layer needs to be optimized in order to have good adhesion to the film. Fully amorphous AlN capping layer deposited at low deposition temperature may result in poor protection. However, high deposition temperature will cause Te evaporation in the $ZrTe_2$ film and crystallization of AlN which may affect the further structural characterization by XRD and TEM. For instance, the sample grown with substrate temperature 600 $^{\circ}$C, protected by the capping layer deposited at 200 $^{\circ}$C shows three orders increase of resistance after exposed in air for 3 days; while for the sample with 250°C grown capping layer, the resistance is stable in air even for a few weeks.

3.2 Structural characterization of thin films grown on sapphire (0001)
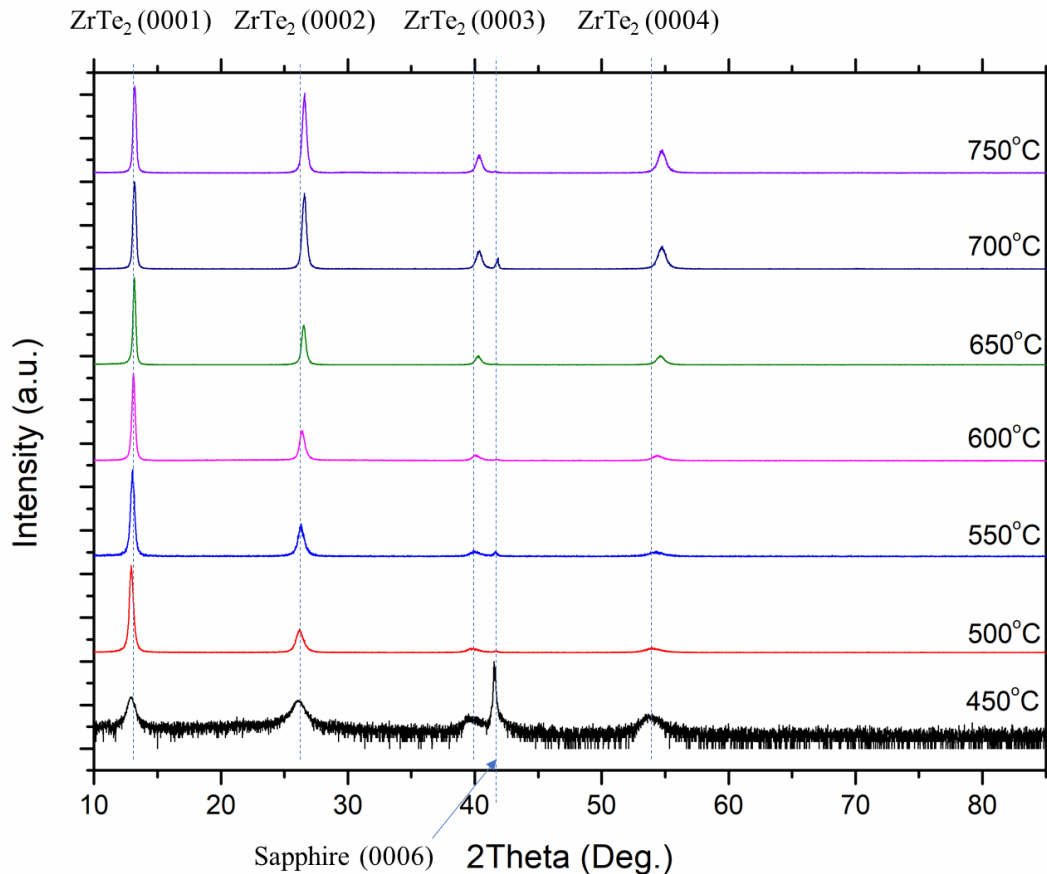
Figure 3-2. XRD pattern of thin films grown on sapphire substrate at different temperatures.

The XRD pattern of thin films grown on sapphire at various temperatures (450 °C to 750 °C) are shown in Figure 3-2 (note that only the pattern of 450 °C grown sample is in log-scale). The dotted lines are introduced to compare the experimental results to the previous research works on $ZrTe_2$ (JCPDS card 54-560).

The intensity of peaks along c direction of $ZrTe_2$ is much higher than that of the substrate peak in a wide range of growth temperature (500 °C to 750 °C), indicating highly crystallized c-orientated $ZrTe_2$. The log-scaled XRD pattern obtained from the 450 °C

grown film is also shown in Figure 3-2; but with significant reduction in intensity for the ZrTe$_2$ (0001) diffraction. This implies that the crystallinity greatly decreases below 450 °C growth temperature, in other words, the growth temperature range of ZrTe$_2$ on sapphire should be from 500 °C to 750 °C.

It is apparent that there is no AlN-crystal-related peak in the diffraction pattern, suggesting that the deposition temperature for Al-N capping layer (200 °C and 250 °C) is not high enough for AlN crystallization or only forms very small nanocrystals.

One may also notice that, the related XRD peaks of ZrTe$_2$ shift right for samples deposited at higher temperature. Here, we proposed that, the right shifts of related XRD peaks for thin films are resulted from the lattice contraction due to the tellurium vacancies induced under thermal treatment at high deposition temperatures.

Several research studies have reported that the tellurium vacancies can be easily found in the telluride compounds after thermal treatment with relatively high temperature because of the low melting point of tellurium elements (~450 °C). [56, 57] This finding supports our hypothesis that the lattice contraction observed in the high temperature grown ZrTe$_2$ is due to the tellurium vacancies. This phenomenon has been well studied in previous research. [58] So, we can conclude that ZrTe$_{2-x}$ thin films are formed for samples with higher deposition temperature. Or we can say, at relatively lower temperatures, ZrTe$_{2+x}$ may be formed.

To further study the microstructure of the ZrTe$_2$ films, cross-sectional TEM observation was carried out for the 550 °C thin film samples grown on (0001) sapphire.

There are two methods for the thin film TEM sample preparation. In this project, as the thin film samples are extremely unstable in air, mechanical polishing and ion milling method mentioned in 0 may not be used because it usually takes a few hours in air or

water. Besides, the hardness of sapphire makes the polishing processes more time-consuming. Thus, the Focused Ion Beam (FIB) is used for the TEM sample preparation. Due to the limitation in electron transmission, the required thickness of TEM specimen should be less than 100 nm. However, the high energy of ion beam in FIB may damage the surface of samples during the preparation process, a protective Pt layer was usually deposited on the sample surface to protect the sample from damage by ion beam.

Then, two hollow regions (yellow blocks in Figure 3-3) are milled using FIB on two sides of the target thin film region, as shown in Figure 3-3. Before the bottom cut and side cut, the specimen is fixed in the sample.

After a few cycles of milling at both sides of the specimen, the specimen become much thinner until it is thinner than 100 nm. Side cut and bottom cut (as shown in Figure 3-4) are used to separate the specimen from the sample and ready to be taken off under optical microscope.
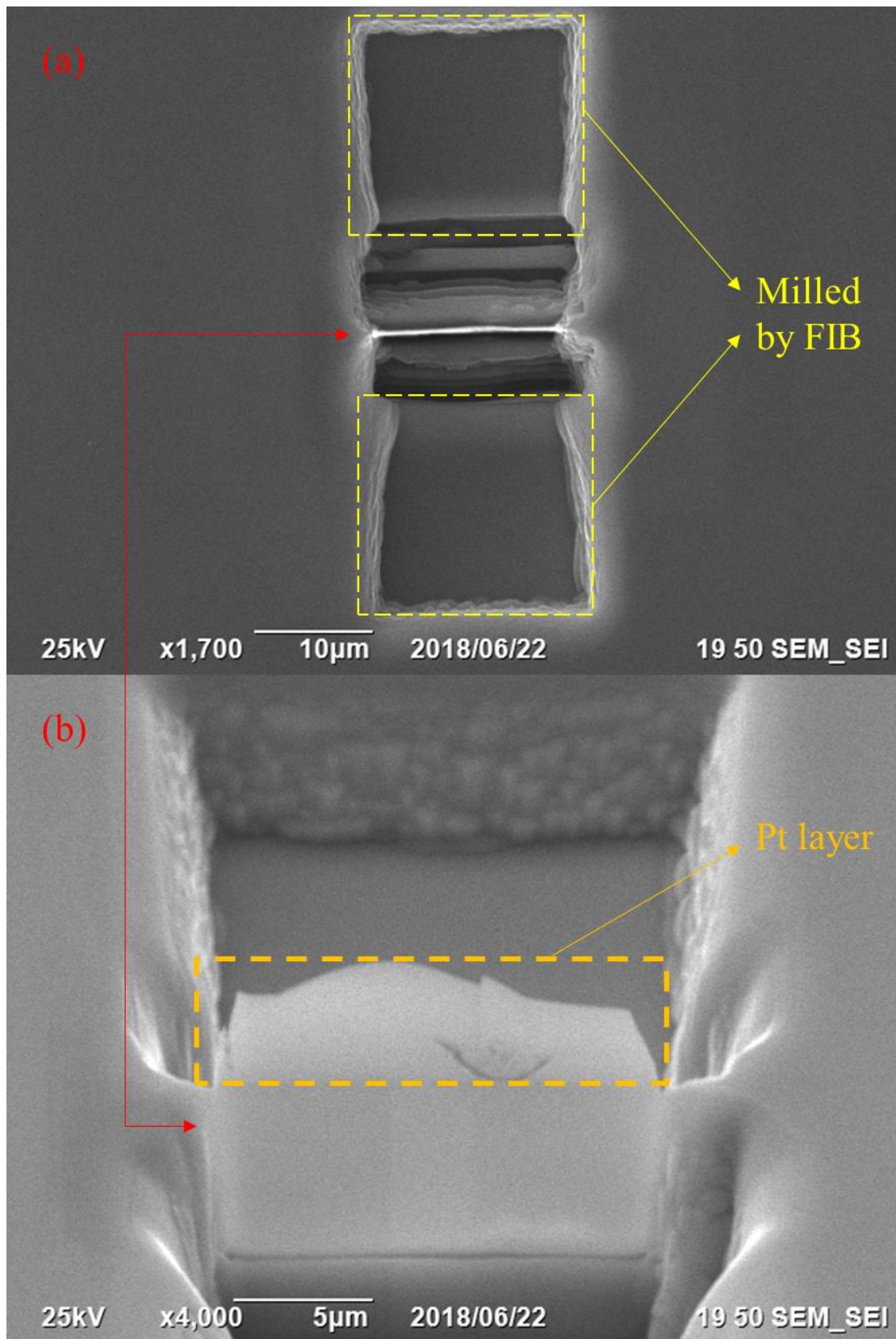
Figure 3-3. FIB processes BEFORE bottom cut and side cut (a) Top view (b) Front view.
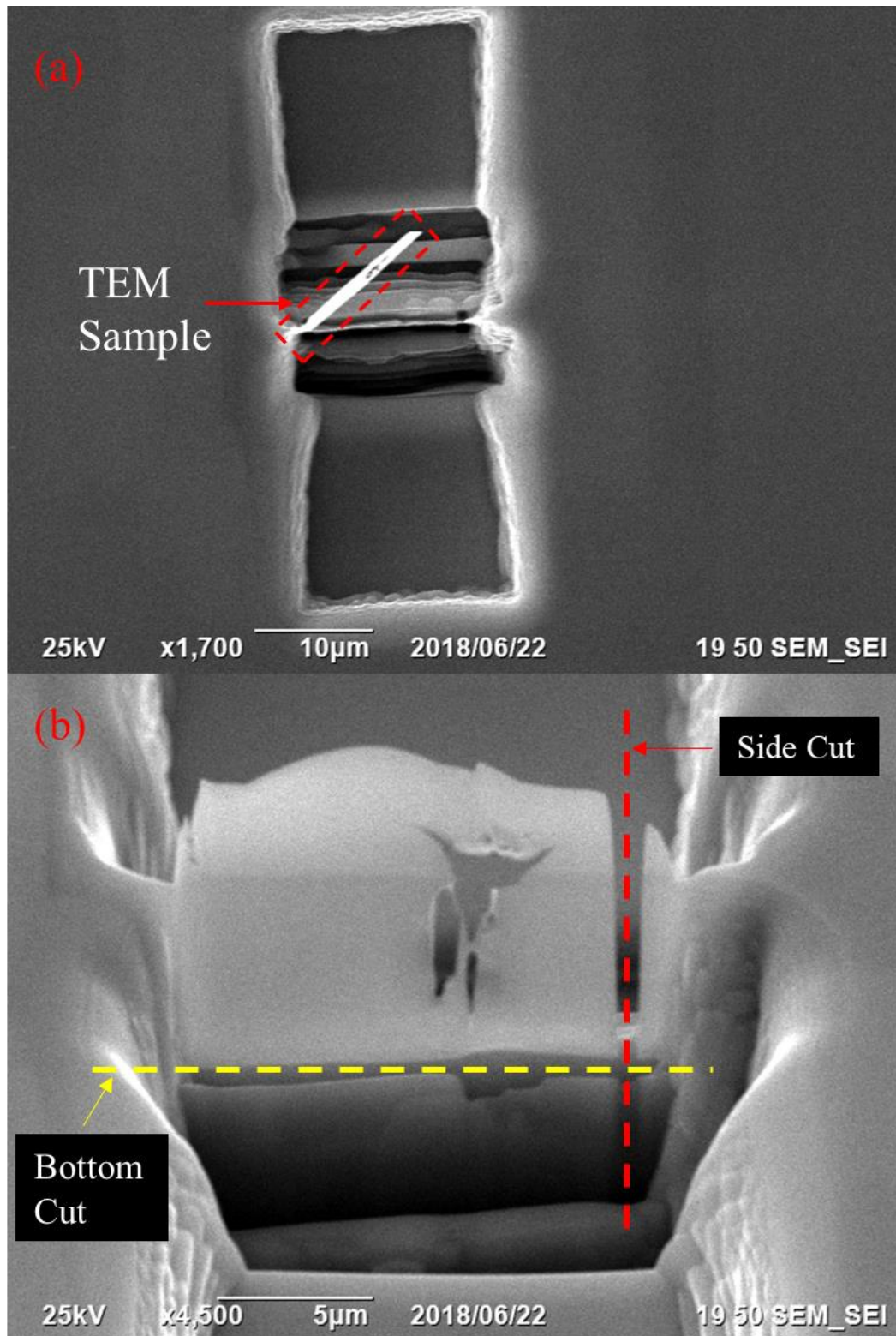
Figure 3-4. FIB processes AFTER bottom cut and one-side cut (a) Top view (b) Front view.
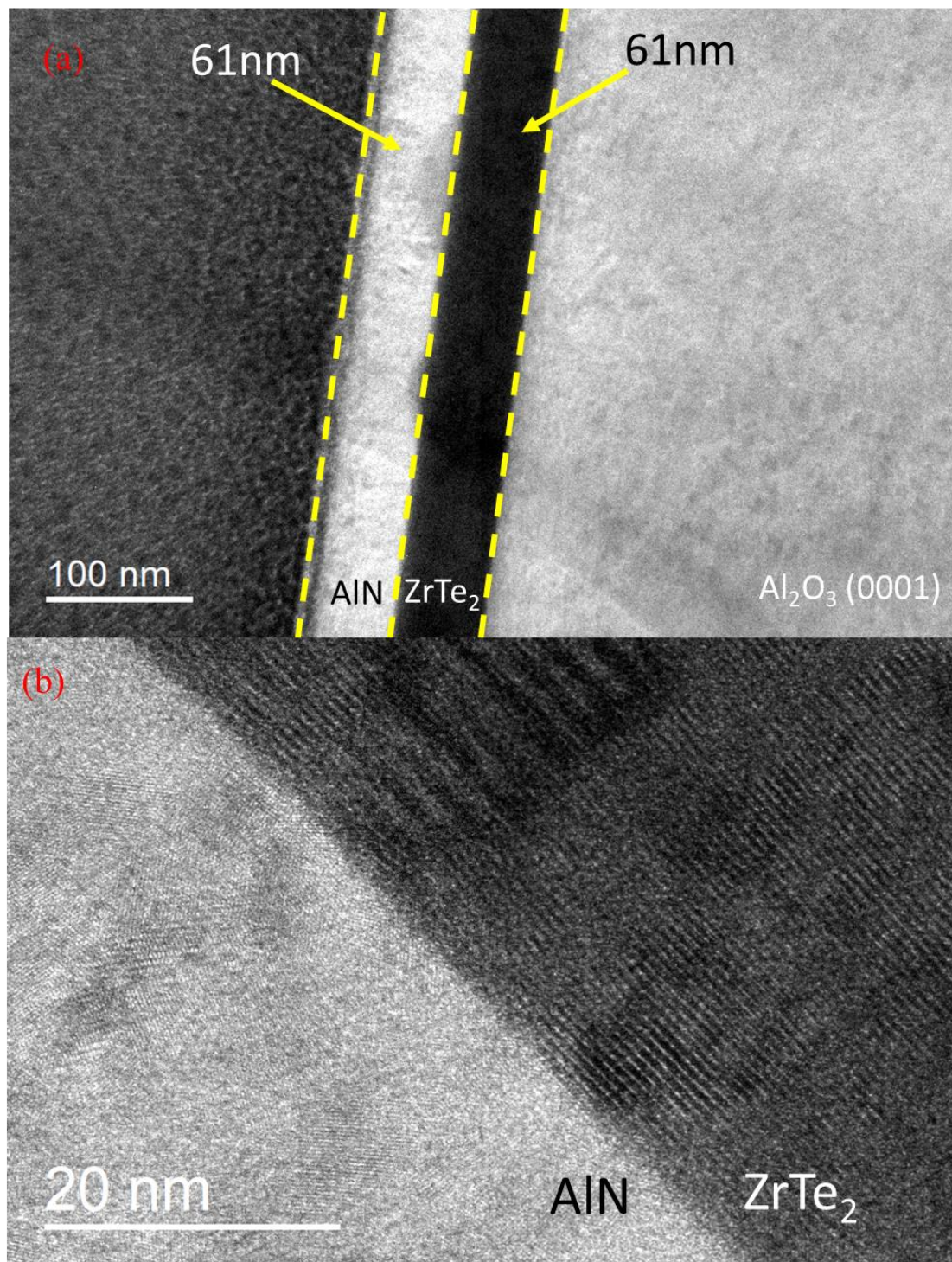
Figure 3-5. Electron Microscopy investigations of thin films grown on Sapphire (0001) at 550 $^{\circ}$C (a) Low-magnification cross-sectional TEM image. (b) High-magnification cross-sectional TEM image showing interface of thin film and Al-N capping layer
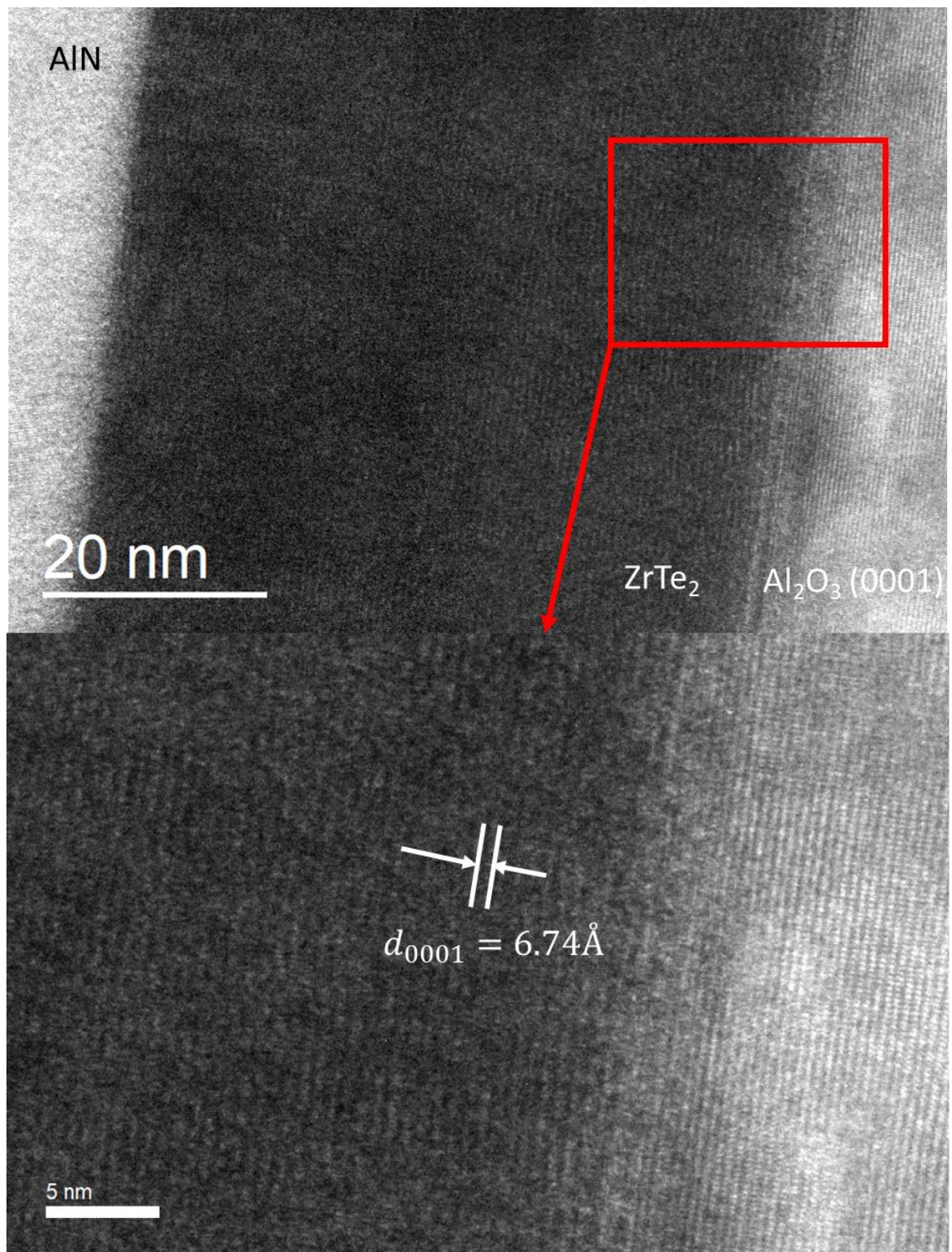
Figure 3-6. High-magnification cross-sectional TEM image of thin film grown on sapphire (0001) at 550 ^{o}C showing ZrTe$_2$ (0001) spacing at the interface.

Figure 3-5 (a) shows the low-magnification cross-sectional TEM image of thin films grown on (0001) sapphire substrate, where one can see that the thickness of both AlN capping layer and $ZrTe_2$ thin film are about 60 nm. Figure 3-5 (b) shows a high uniformity of the thin film with negligible roughness, which may be an indication of epitaxial growth of $ZrTe_2$ thin film on sapphire substrate. It is also apparent that polycrystalline AlN capping is formed. High-resolution TEM (HRTEM) images of this sample are shown in Figure 3-6. The measured d-spacing parallel to the substrate surface is equal to 6.74 Å, which matches with XRD peak corresponding to $ZrTe_2$ (0001). This d-spacing provides another evidence to support our proposed explanation of lattice expansion along c-axis. Combining the results from XRD measurement and HRTEM studies, we claim that a high-quality and large area $ZrTe_2$ thin film has been epitaxially grown, along c-axis, on sapphire substrate with high surface uniformity.
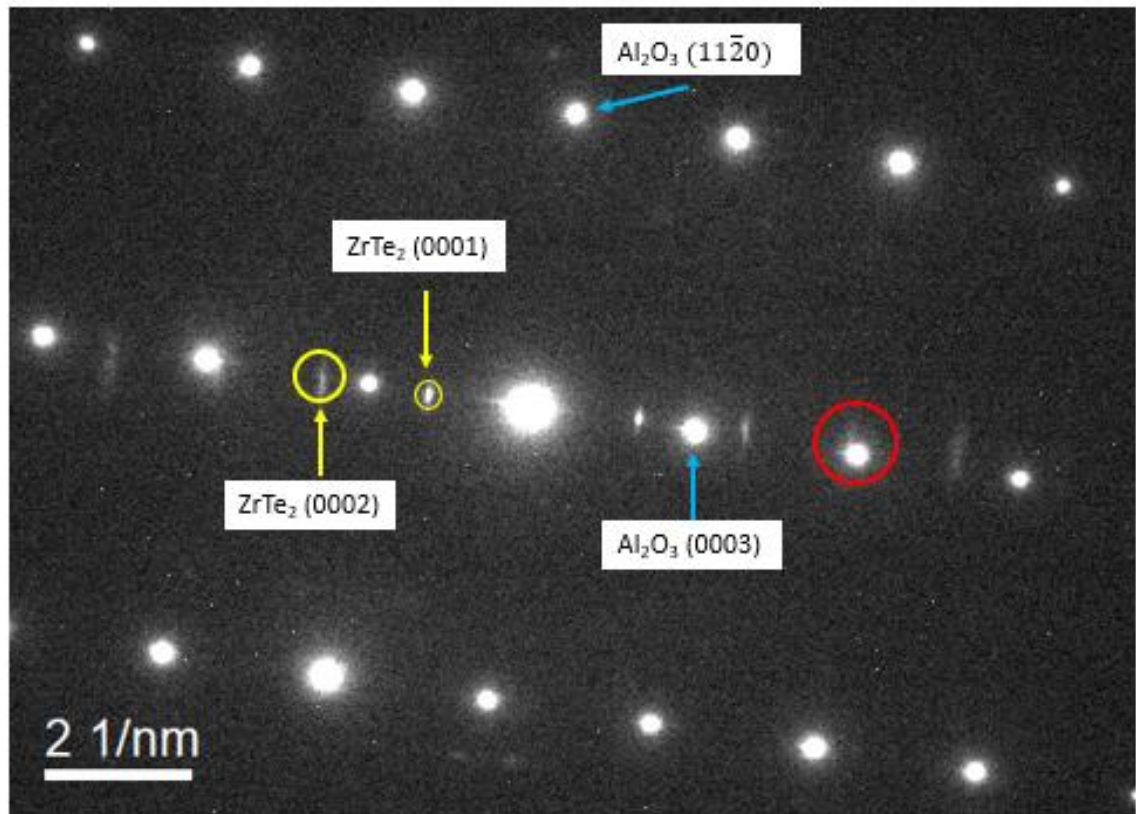
Figure 3-7. Selected Area Electron Diffraction (SAED) pattern taken at both the film (550°C grown) and the sapphire (0001) substrate.

Figure 3-7 shows the SAED pattern taken from the region including the thin film and sapphire (0001) substrate. Similarly, according to the diffraction spot and their index, the thin film and sapphire substrate have a crystallographic orientation relationship of $(0001)_{ZrTe_2}$ // $(0001)_{Al2O3}$, which exactly match with our XRD results. However, as the d-spacing of $ZrTe_2$ (0003) and sapphire (0006) are very close with each other, their diffraction spots are overlapped at red circle in Figure 3-7.

(a)

(b)

Al_2O_3 $(10\bar{1}2)$ // $ZrTe_2$ $(10\bar{1}2)$
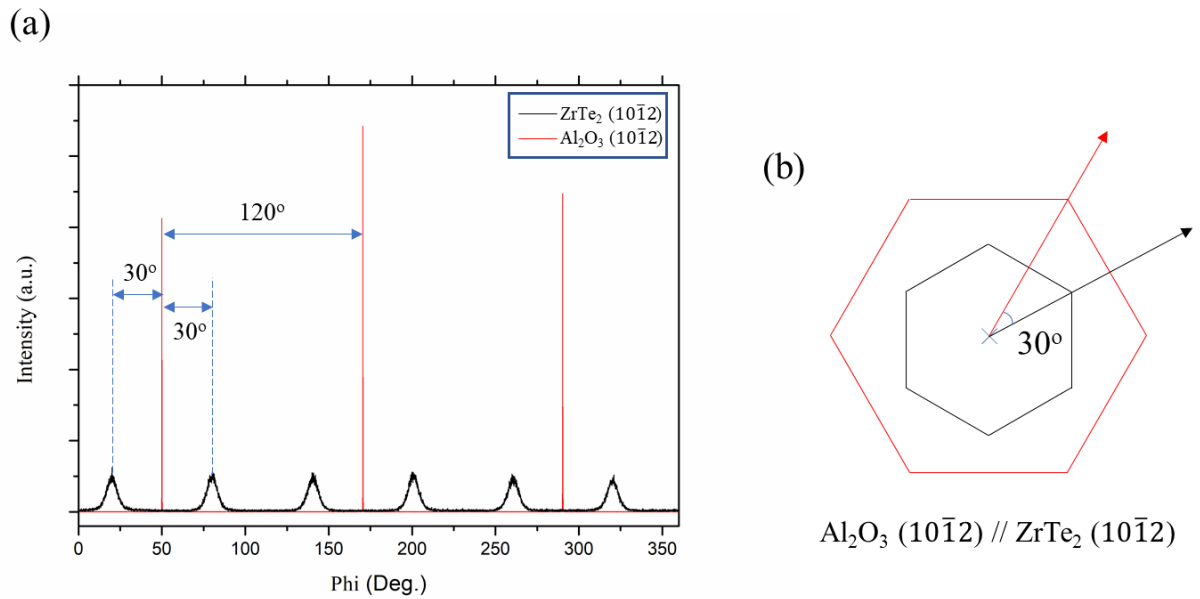
Figure 3-8. (a) ∅ - scan of 750 °C grown samples on sapphire (0001) substrate. (b) Schematic diagram of (0001) projection of ZrTe₂ grown on sapphire (0001).

In order to study the orientation relationship between thin film and substrate along the x-axis, ∅-scan of XRD for 750 °C grown samples on sapphire (0001) was also measured. The ∅-scan of $(10\bar{1}2)$ plane (also called r-plane) of both $ZrTe_2$ thin film and sapphire substrate was selected. Three Al_2O_3 $(10\bar{1}2)$ peaks separated by 120° in Figure 3-8 (a) show the trigonal space symmetry of a sapphire crystal, while six $ZrTe_2$ $(10\bar{1}2)$ peaks separated by 60° show the hexagonal space symmetry of a hexagonal $ZrTe_2$ thin film. The peak positions of $ZrTe_2$ and sapphire are separated by 30° implying that there is a 30° rotation between the intersections of the scanning family with a surface of $ZrTe_2$ and sapphire (see Figure 3-8 (b)). So, the in-plane orientation relationship is $[11\bar{2}0]_{ZrTe2}$ // $[01\bar{1}0]_{sapphire}$.

3.3 Transport properties of thin film samples on (0001) sapphire

Refer back to Figure 2-15 and Figure 2-16, to measure the transport properties and some electrical parameter of thin film samples using PPMS, the dimensions of thin film samples and the distance between electrodes should be recorded. For example, the distance between voltage terminals in R-T measurement (s); the distance between hall voltage terminals in Hall-measurement (d); the width of the thin film sample (w) and the thickness of the thin film (t).
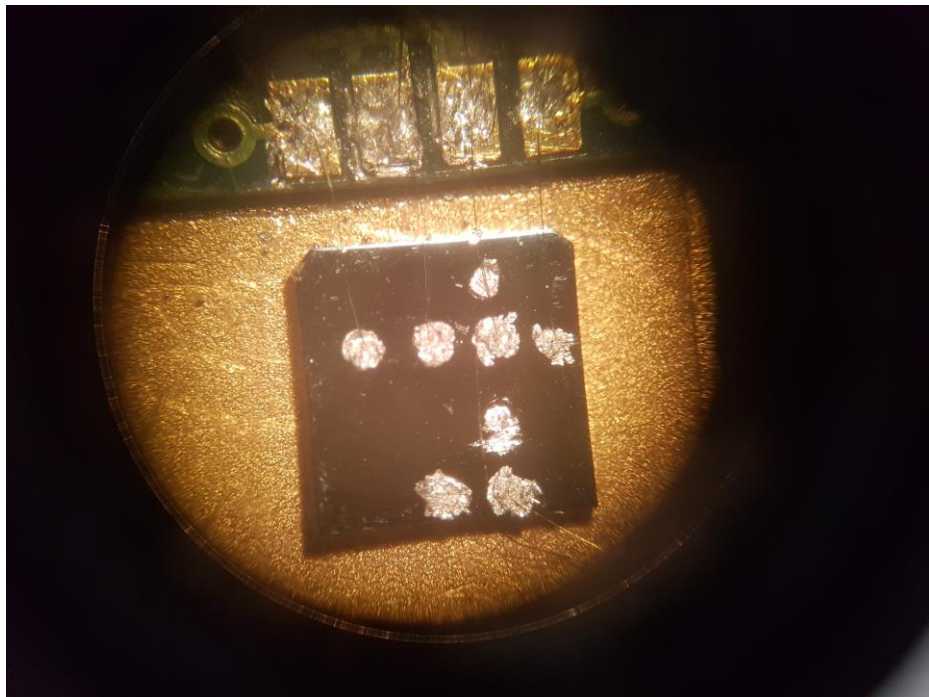
Figure 3-9. Microscale indium balls pressed on samples' surface as surface electrode.

3.3.1 Performance of the protective Al-N capping layer

Besides the protection from air, electrical insulation is also an important requirement when selecting the capping layer. In this project, polycrystalline AlN capping layer was used to protect the thin films sample from contacting with air and moisture. Polycrystalline AlN is an electrical insulator, so the electrical transport properties measurements should not be affected by the capping layer.

As mentioned in Chapter 3, before applying the AlN capping layer, a great increase in resistance of thin film samples is found after exposing the samples in air for one hour. Similar result was found in the very beginning of R-T measurement to the films without AlN capping layer using PPMS.

For the 700 ℃ thin film grown on sapphire substrate without any capping layer, the resistivity was measured as 0.75 $m\Omega \cdot cm$ at 300 K in the R-T measurement right after the deposition using PLD. Unexpectedly, in the 2nd measurement for the same sample after a sample preparation process with duration about 30 minutes, the resistivity show a great increase to 3.2 $\Omega \cdot m$ at 2K, as shown in Figure 3-10.
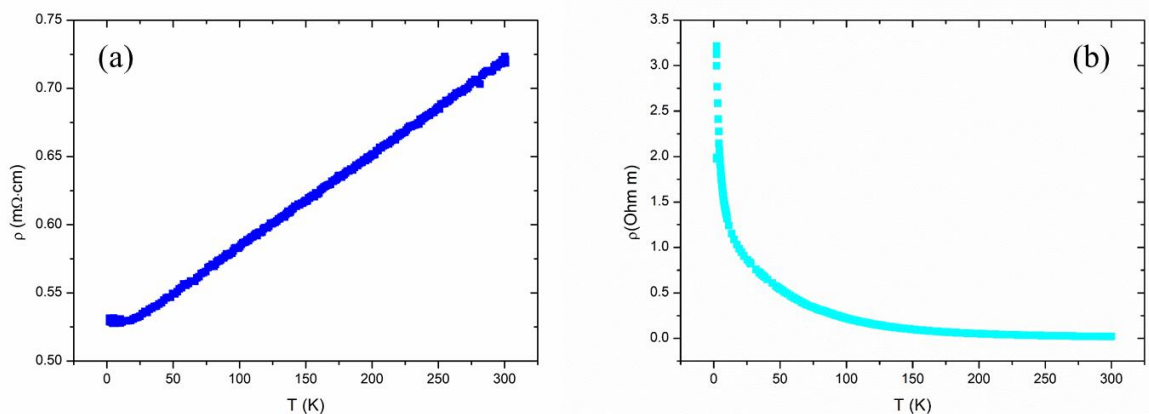
Figure 3-10. $\boldsymbol{\rho}$**-T Measurement of 700 ℃ thin film sample grown on sapphire without capping layer. (a) before exposing in air for 30 minutes (b) after exposing in air for 30 minutes**

In contrast, for thin film samples covered by the polycrystalline AlN capping layer, stable transport properties of thin films can be achieved and the results in different measurement cycles are consistent and repeatable for each sample, indicating outstanding protection for $ZrTe_2$ thin films.

3.3.2 ρ-T Characteristics

To study temperature-dependent resistivity of the ZrTe$_2$ thin films on (0001) sapphire, the resistivity of the thin films grown at 450, 500, 550, 650, 700 and 750 $^{\circ}$C were measured at temperatures from 300 K to 2 K as shown in Figure 3-11. It is apparent that all the ZrTe$_2$ thin films show typical metallic or semimetal characteristic. But one should notice that the resistance change from room temperature to 2 K is not significant.
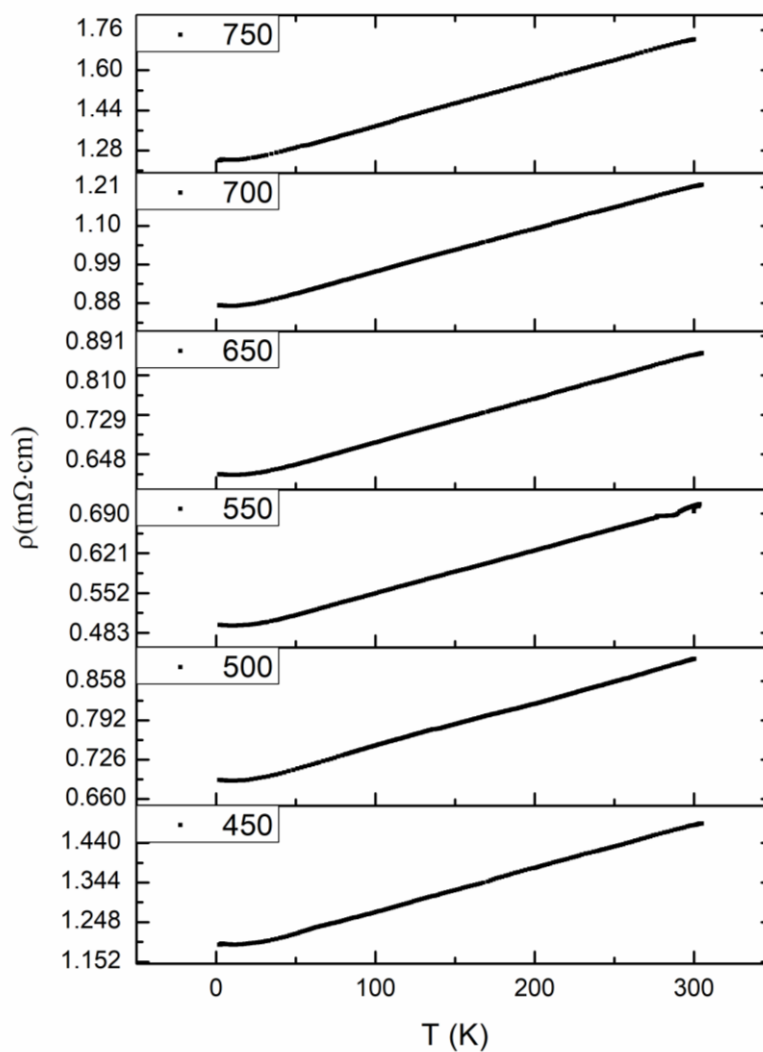
Figure 3-11. ρ-T measurement of thin film on sapphire substrate at different growth temperature.

3.3.3 Magnetoresistance Characteristic (MR)
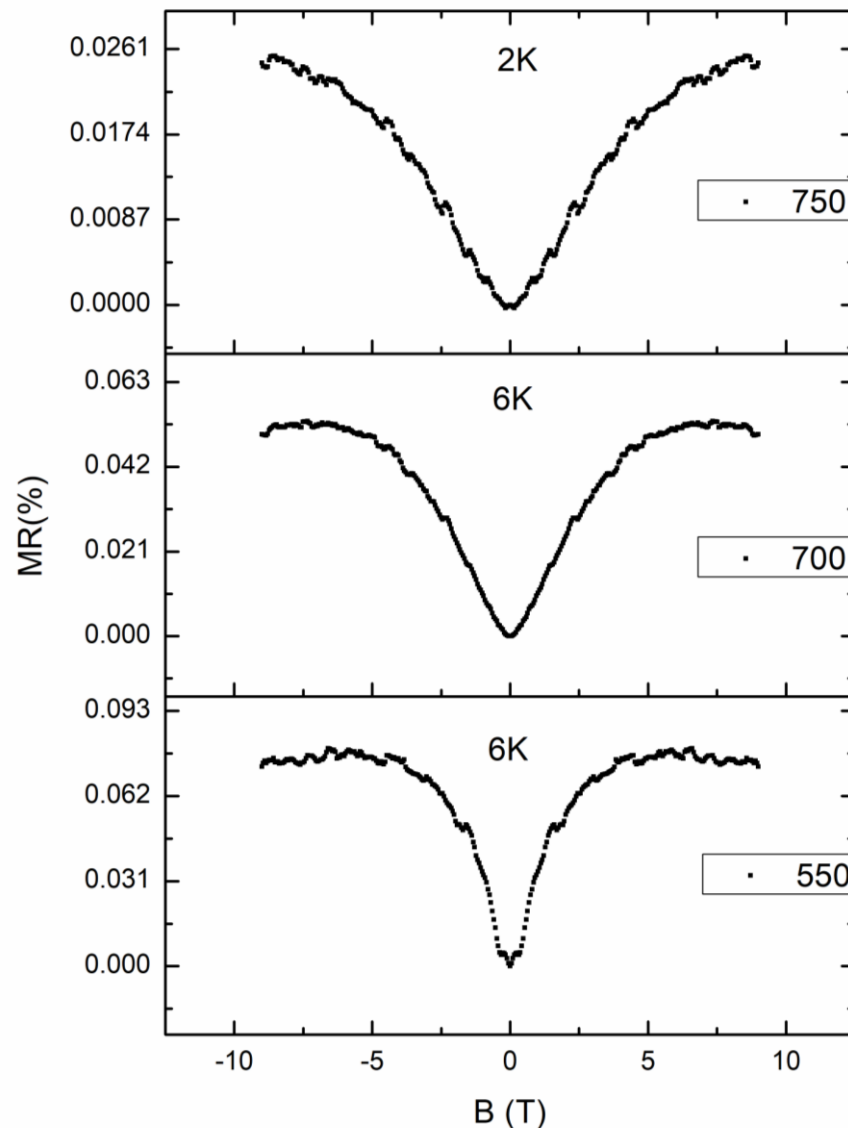
Figure 3-12. MR measurement of sapphire substrate samples. (a) 750 °C grown temperature measured at 2 K (b) 700 °C grown temperature measured at 6 K (c) 550 °C grown temperature measured at 6 K. The magnetic field is perpendicular to the film.

Figure 3-12 shows some of the MR measurements of $ZrTe_2$ thin film samples with different growth temperatures. It can be seen that when the magnetic field is perpendicular to the film, all samples show very similar result with very small and positive MR.

According to the report by Tsipas (2018) based on Angle Resolved Photoemission Spectroscopy (ARPES) measurement, monolayer or a few layers $ZrTe_2$ grown on InAs (111) was proven to be Dirac semimetal with very large MR effect [16]. Our MR result does not seem to be the case. However, due to the Dirac-like cone in 2-dimensions at the zone center caused by the linear dispersion in ARPES, Tsipas also suggested that monolayer $ZrTe_2$ could be considered as the electronic analogue of graphene. From the difference between graphite and graphene, graphene is considered as having a dimensional-dependency in its transport properties, it is suggested that $ZrTe_2$ transport properties may exhibit dimensional-dependency. The unexpected MR measurement results from our $ZrTe_2$ thin films are about ~60 nm thick, so monolayer or a few-layer thick $ZrTe_2$ on sapphire deserves further study.

3.3.4 Hall Characteristics

Hall measurement was conducted to characterize the carrier density and mobility of the thin film samples. 3.3.3 shows the Hall resistance as a function of external magnetic field for the 550 °C grown sample on sapphire substrate. Based on these results, the carrier density and mobility of the ZrTe$_2$ thin film on sapphire can be obtained.
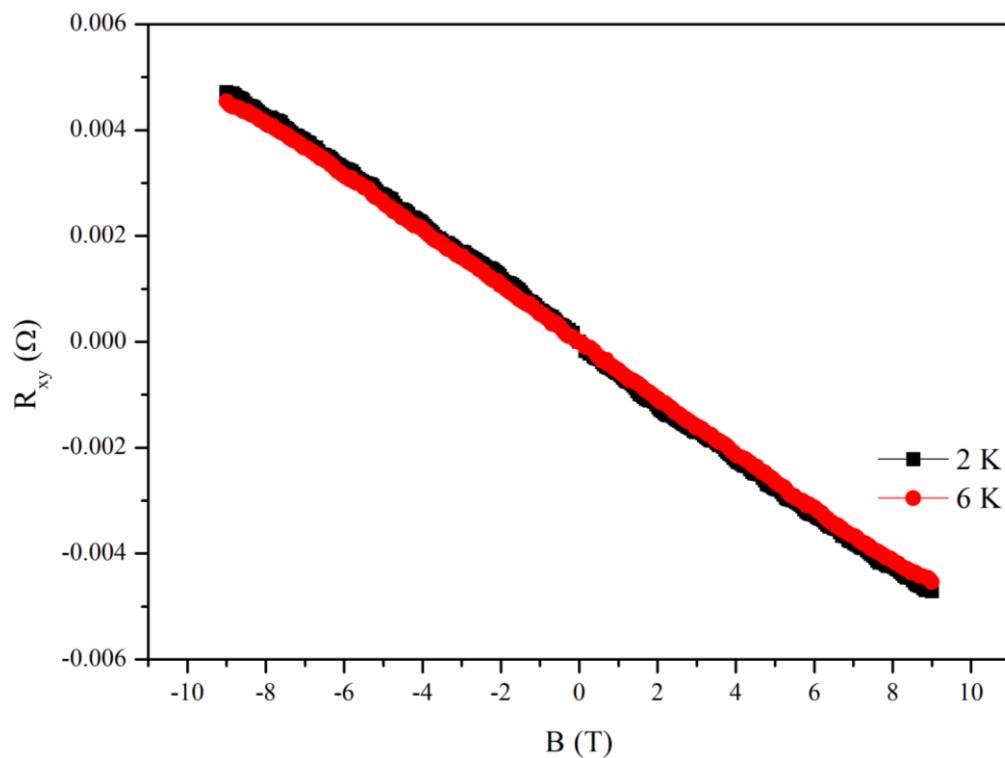
Figure 3-13. Hall resistance – External magnetic field (R$_{xy}$ – B) measurement of 550 °C sample grown on sapphire substrate at 2 K and 6 K.

Carrier density, n_s, of thin films can be estimated using

$$n_s = \frac{IB}{qtV_H}$$

where I is the current, B is the magnetic field induction, q is the carrier charge, V$_H$ is the Hall voltage and t is the thickness of thin film. In our ZrTe$_2$ film, the linear behavior and the negative slope of R$_{xy}$ – B indicate that there are only electron carriers. The thickness of the thin film, t, is taken as 60 nm which is measured from the TEM image as we

mentioned in 3.2.

Thus, combining the equation with $R_{xy} = \frac{V_H}{I}$, we have

$$n_s = \frac{B}{etR_{xy}}$$

From the measurement of hall resistance versus external magnetic field, we can estimate

the values of $\frac{R_{xy}}{B}$ by simply calculating the slope of the curve. The estimated values of

electron carrier densities of 550 °C grown ZrTe$_2$ film at 2 K and 6 K are 1.963×10^{29} m^{-3}

and 2.0395×10^{29} m^{-3}, respectively.

Meanwhile, the carrier mobility of ZrTe$_2$ thin film samples can be calculated by

$$\mu = -\frac{\sigma V_H t}{IB} = -\frac{\sigma}{n_s e}$$

where I is the current source, B is the external magnetic field, σ, the conductivity of thin

film, V$_H$, Hall voltage and t is the thickness of thin film. Similar to the calculation of the

carrier density, the values of $\frac{V_H}{IB}$ can be estimated by measuring the slope of the curve.

The conductivity of thin film, σ, can be calculated using $\sigma = \frac{1}{\rho}$, where ρ is the

resistivity of thin film measured in the R-T measurement, which is 7.245×10^{-6} $\Omega \cdot$ m at

2 K and 7.23×10^{-6} $\Omega \cdot$ m at 6 K. So, the calculated values of electron carrier mobilities

of 550 °C grown film on sapphire at 2 K and 6 K are 4.386×10^{-2} cm^2/Vs and 4.2322×10^{-2} cm^2/Vs, respectively.

The high electron carrier density implies that the Fermi level is much higher than the

Dirac point and thus the properties of massless Dirac fermions cannot be observed. This

is consistent to the low mobility obtained from the hall measurement.

Large MR effect is commonly observed in typical Dirac or Weyl semimetals, such as

WTe$_2$ [59], in which the extremely large MR was attributed to the compensation of holes

and electrons. Combined with the linear dependence of Hall resistance on external magnetic field, the observed small MR effect in our R-T measurements probably due to the overwhelming dominance of classical electrons.

3.4 Summary

In summary, epitaxial growth of $ZrTe_2$ on (0001) sapphire substrate has been realized by PLD with $ZrTe_5$ target. The transport properties of the thin $ZrTe_2$ films have been characterized by PPMS, and the results show metallic conduction of the film with small MR and high carrier density.

CHAPTER 4 PULSED-LASER DEPOSITION OF ZrTe$_2$ THIN FILMS ON (110) STO

From the results mentioned in Chapter 3, we found that the hexagonal ZrTe$_2$ thin films are epitaxially grown on hexagonal (0001) sapphire substrate with orientation relationship of (0001)$_{ZrTe2}$ // (0001)$_{Al2O3}$ and [11$\bar{2}$0]$_{ZrTe2}$//[01$\bar{1}$0] $_{Al2O3}$. However, we could not see any sign of non-trivial transport property that could be related to topological semimetal or Dirac fermion in the film. Since SrTiO$_3$ has been used in many researches works as substrate for variety kind of thin films, it was also selected as substrate for zirconium telluride thin film study.

4.1 Thin Film Synthesis Experiment

Table 4-1. PLD Deposition Condition of Thin Films on STO (110).

Samples	(Zr-Te) Substrate Temperature (°C)	Laser Parameter on Zr-Te Target	(Al-N) Substrate Temperature (°C)	Laser Parameter on Al-N Target
1	450	5Hz, 10mins, 250mJ	250	5Hz, 30mins, 300mJ
2	500	5Hz, 10mins, 250mJ	250	5Hz, 30mins, 300mJ
3	550	5Hz, 10mins, 250mJ	250	5Hz, 30mins, 300mJ
4	580	5Hz, 10mins, 250mJ	250	5Hz, 30mins, 300mJ
5	600	5Hz, 10mins, 250mJ	200	5Hz, 30mins, 300mJ

Same target, Zr-Te (molar ratio = 1:5) was also used for the thin film deposition on STO by PLD. Same deposition parameters were used for the thin film deposition on (110) STO to compare the growth mechanism of ZrTe$_2$ thin films grown on (0001) sapphire and (110)

STO substrate. In fact, different substrates were put together when growing zirconium telluride thin films.

4.2 Structural characterizations of thin films grown on (110) STO
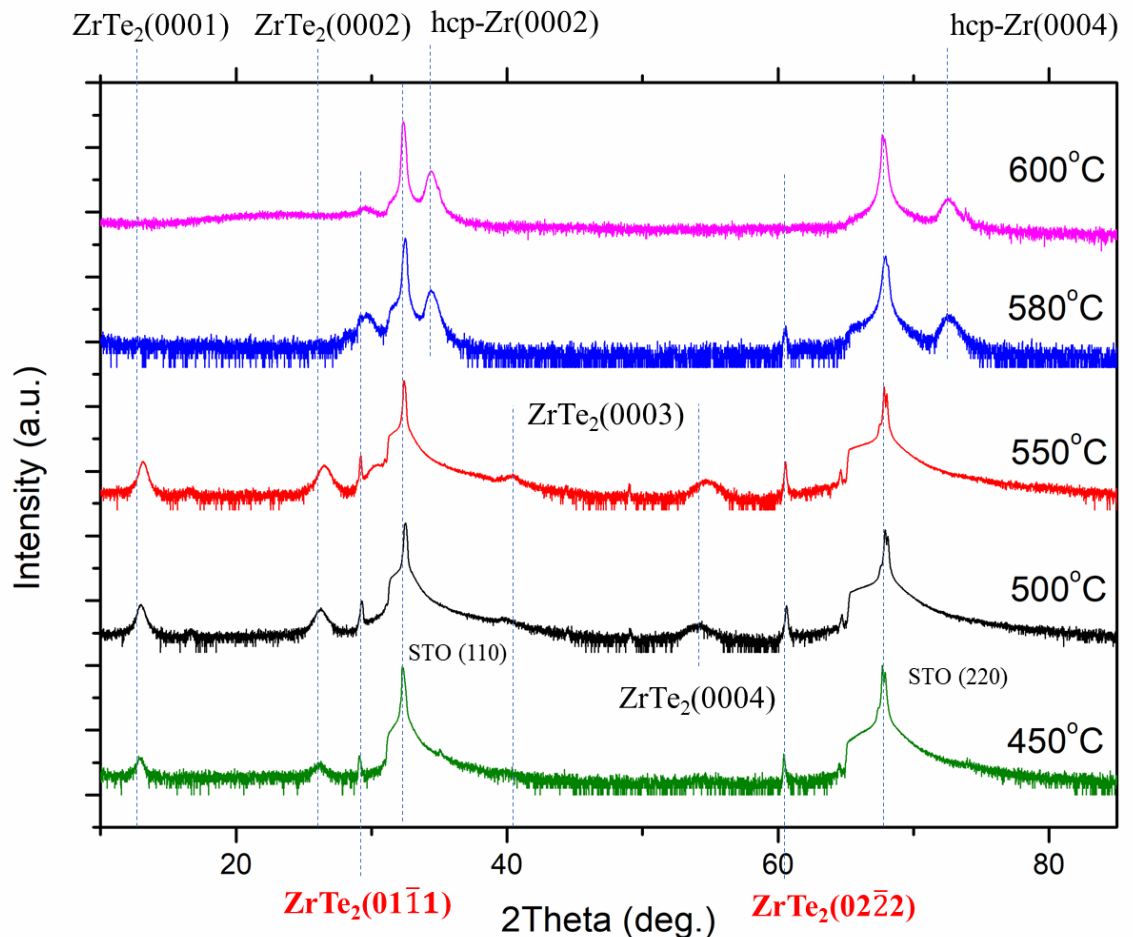
Figure 4-1 Log-scaled XRD pattern of thin films grown on STO (110) with various growth temperatures.

In Figure 4-1, the out of plane XRD pattern for samples with various growth temperatures are shown. In general, the peaks representing (0001), (0002), (0003), (0004) diffraction plane of $ZrTe_2$ can be observed easily for samples grown at substrate temperatures within 450 ºC to 550 ºC. This result suggests that the z-axis oriented $ZrTe_2$ dominates the thin

films growth at this range of temperatures. The increased intensity of $ZrTe_2$ (0001) peak at higher temperatures indicates that the crystallinity of the films at higher temperature is higher than the films grown at lower temperatures. One can see that for the film grown at 450 °C, the peak corresponding to $ZrTe_2$ (0004) becomes almost invisible, suggesting lower crystallinity for the low temperature grown film.

One should also notice that there are a few weak peaks observed at ~29.3° and ~60.4° besides the main $(000l)$ peaks. These peaks roughly match $ZrTe_2$ $(01\bar{1}1)$ and $ZrTe_2$ $(02\bar{2}2)$, suggesting that there might be another orientation of $ZrTe_2$ thin film or a second phase different from $ZrTe_2$ formed in the deposition. This will be further discussed in later sessions.

The dotted lines are introduced to compare the experimental results to the previous research works on $ZrTe_2$ (JCPDS card 54-560) and hex-Zr (JCPDS card 2-821). Different from the obtained XRD pattern of thin films on (0001) sapphire, the intensities of peaks related to c-orientation planes of $ZrTe_2$ are much lower than that of the substrate peak in a wide range of growth temperatures (450 °C to 550 °C). This observation suggests that the crystallinity of the z-orientated $ZrTe_2$ could be lower compared to the film grown on sapphire substrate. This difference may be due to the crystal structure matching that both $ZrTe_2$ and sapphire are in hexagonal structure, while STO is in cubic structure, so it is more favorable for the epitaxial growth of $ZrTe_2$ on sapphire (0001) substrate but not on (110) STO substrate.

It is worthy to point out that, the phenomenon of right shift for the XRD peaks corresponding to the higher temperature grown $ZrTe_2$ films on STO substrate is similar to that on sapphire substrates. However, different from the sapphire substrate, the XRD

results show that, when the growth temperature is higher than 580 °C, the films on STO substrate is Zr instead of $ZrTe_2$, while the peaks indicating hexagonal zirconium (0002) and (0004) samples are absent. This provides a strong evidence that Te atoms are evaporated due to the high substrate temperature.

Nevertheless, the small peaks that could be from $ZrTe_2$ $(01\bar{1}1)$ and $(02\bar{2}2)$ planes still present in the XRD pattern from samples grown at temperatures higher than 580 °C. This implies that there is a $ZrTe_2$ thin film grown from $(01\bar{1}1)$ direction parallel to the (110) direction of STO substrate even under high-temperature thermal treatment, but still with peak right shifted resulted from lattice contraction. However, since these peaks may also be labeled as (0001) oriented ZrTe, it is more reasonable to believe that these small peaks should be from ZrTe instead of $ZrTe_2$. Between $ZeTe_2$ and Zr, there should be a window for ZrTe phase formation.

Based on the above analysis, we proposed the growth model as shown in Figure 4-2. Between hex-Zr and STO substrate for samples with grown temperature higher than 580 °C, the film grown is ZrTe/Zr (see Figure 4-2 (a)). While the structure of thin film samples on STO (110) with grown temperature between 450 °C and 550 °C is shown in Figure 4-2 (b).

(a)

Al-N Capping Layer

Hex-Zr (0001)
ZrTe$_2$ (01$\bar{1}$1)

STO (110)

(b)

Al-N Capping Layer

ZrTe$_2$ (0001)
ZrTe$_2$ (01$\bar{1}$1)
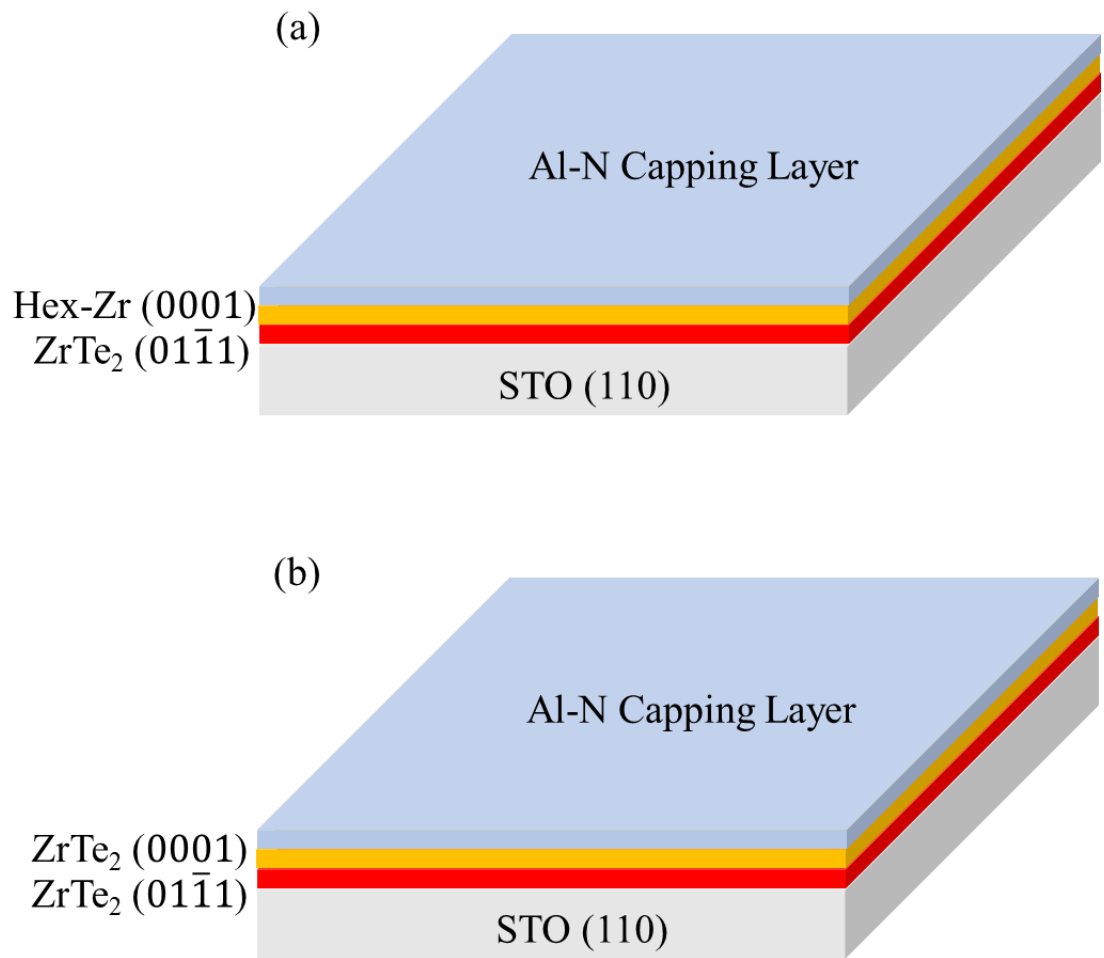
STO (110)

Figure 4-2. Structure of thin film samples on STO (110) (a) with growth temperature

higher than 580 $^{\circ}$C. (b) with grown temperature between 450 $^{\circ}$C to 550 $^{\circ}$C.
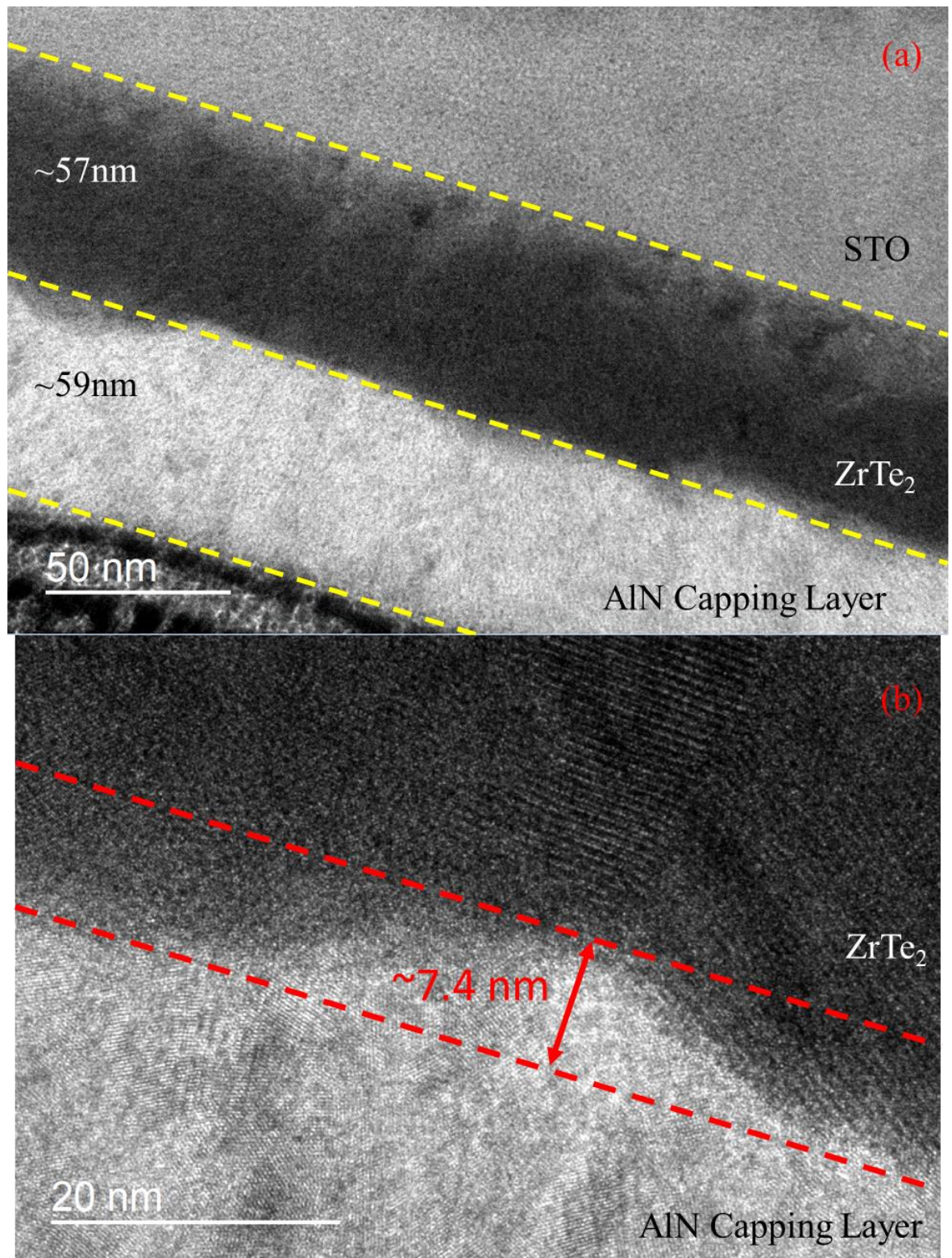
Figure 4-3. Electron Microscopy investigations of thin films grown on STO (110) at 550 $^{\circ}$C.

(a and b) Low-magnification cross-sectional TEM image. (Prepared using FIB)
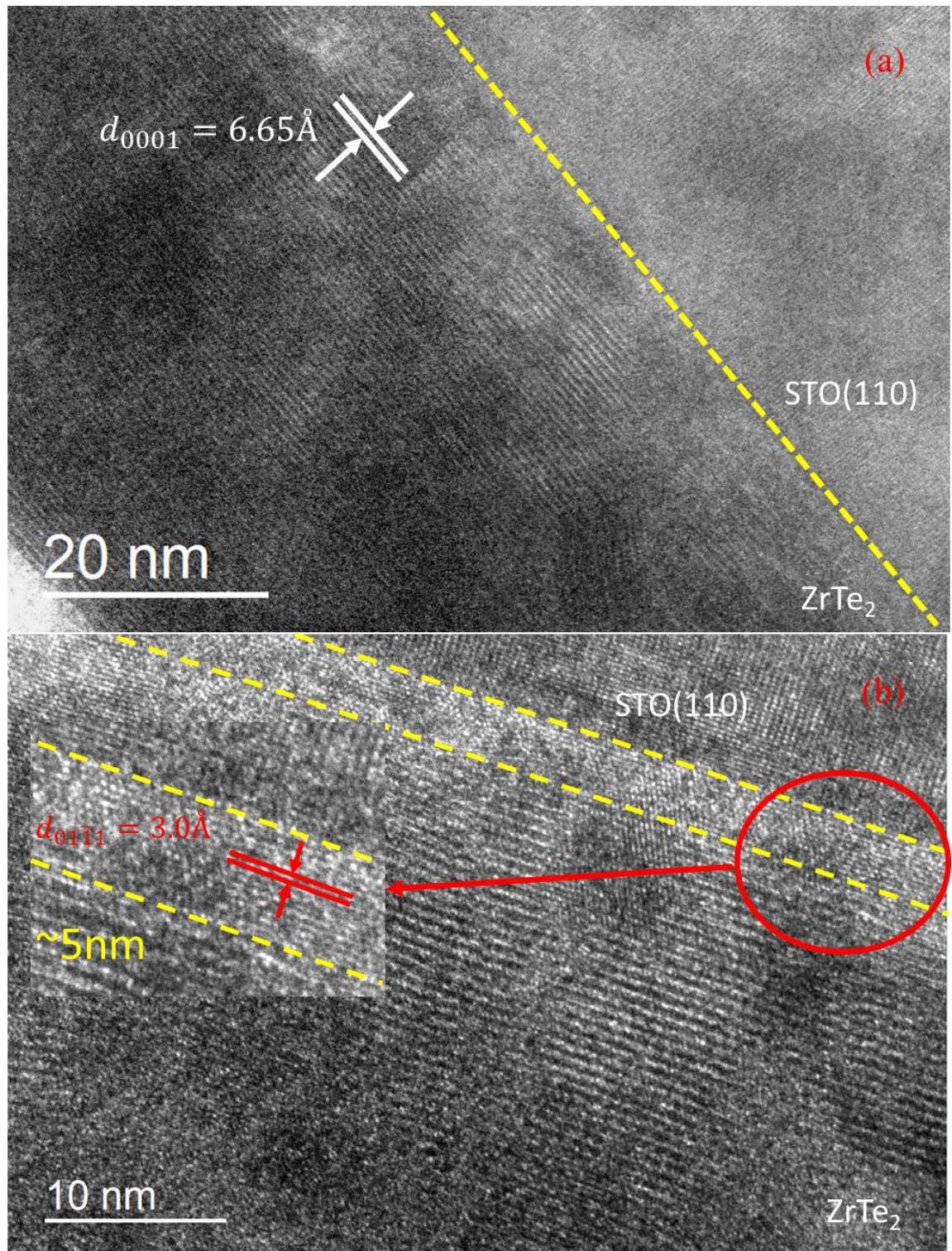
Figure 4-4. Electron Microscopy investigations of thin films grown on STO (110) at 550 °C.

(a and b) High-magnification cross-sectional TEM image showing ZrTe$_2$ (01$\bar{1}$1) spacing at

the interface. (Prepared using FIB)

Generally, growth temperature and substrate selection will determine the growth orientation of thin films, however, the XRD results show growth of highly oriented c-axis $ZrTe_2$ on STO substrates. Figure 4-3 (a) and (b) show the low-magnification cross-sectional view of the thin film sample grown on (110) STO at 550 ºC prepared using FIB. It can be seen that the thickness of $ZrTe_2$ thin film and Al-N capping layer is about 57 nm and 59 nm, respectively. Figure 4-3 (b) shows the interface of $ZrTe_2$ thin film and Al-N capping layer, in which the uniformity of thin film is relatively low with roughness about 7.4 nm. It can also be seen that the AlN capping layer forms polycrystalline structure at 250 ºC growth temperature.

The high-resolution TEM (HRTEM) images of this sample are shown in Figure 4-4 (a) and (b). One can see that the $ZrTe_2$ film is highly c-axis oriented layered structure, except a 5 nm-thick uniform layer at the interface between the $ZrTe_2$ thin film and STO substrate. A measured lattice spacing of 3.0 Å suggests that this layer could be $(01\bar{1}1)$ orientated $ZrTe_2$ or (0002) lattice spacing of ZrTe, suggesting that this interfacial layer may also be ZrTe.

Combining the results of XRD measurement and HRTEM studies, we can confirm that on (110) STO substrate the (0001) is the dominated orientation for the $ZrTe_2$ thin film growth, together with a 5 nm-thick interfacial layer which could be $ZrTe_2$ $(01\bar{1}1)$ or ZrTe (0002).
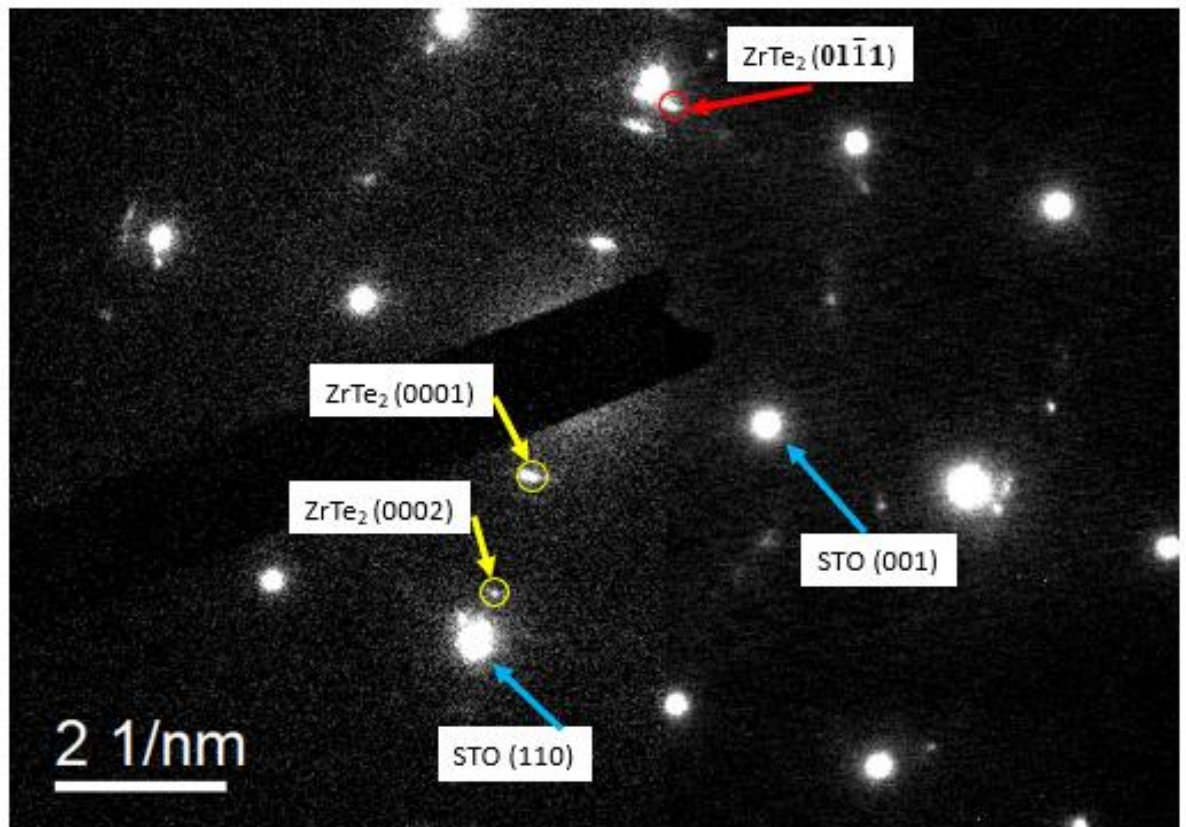
Figure 4-5. Selected Area Electron Diffraction (SAED) pattern of the film (550 ^{o}C grown) and the STO (110) substrate.

Figure 4-5 shows the SAED pattern taken from the region including the thin film and STO (110) substrate, where certain orientation relationship between thin film and substrate can be observed. According to the diffraction spot and their index, the thin film and STO substrate have a crystallographic orientation relationship of $(0001)_{ZrTe2}$ // $(110)_{STO}$ which matches well to the XRD results.
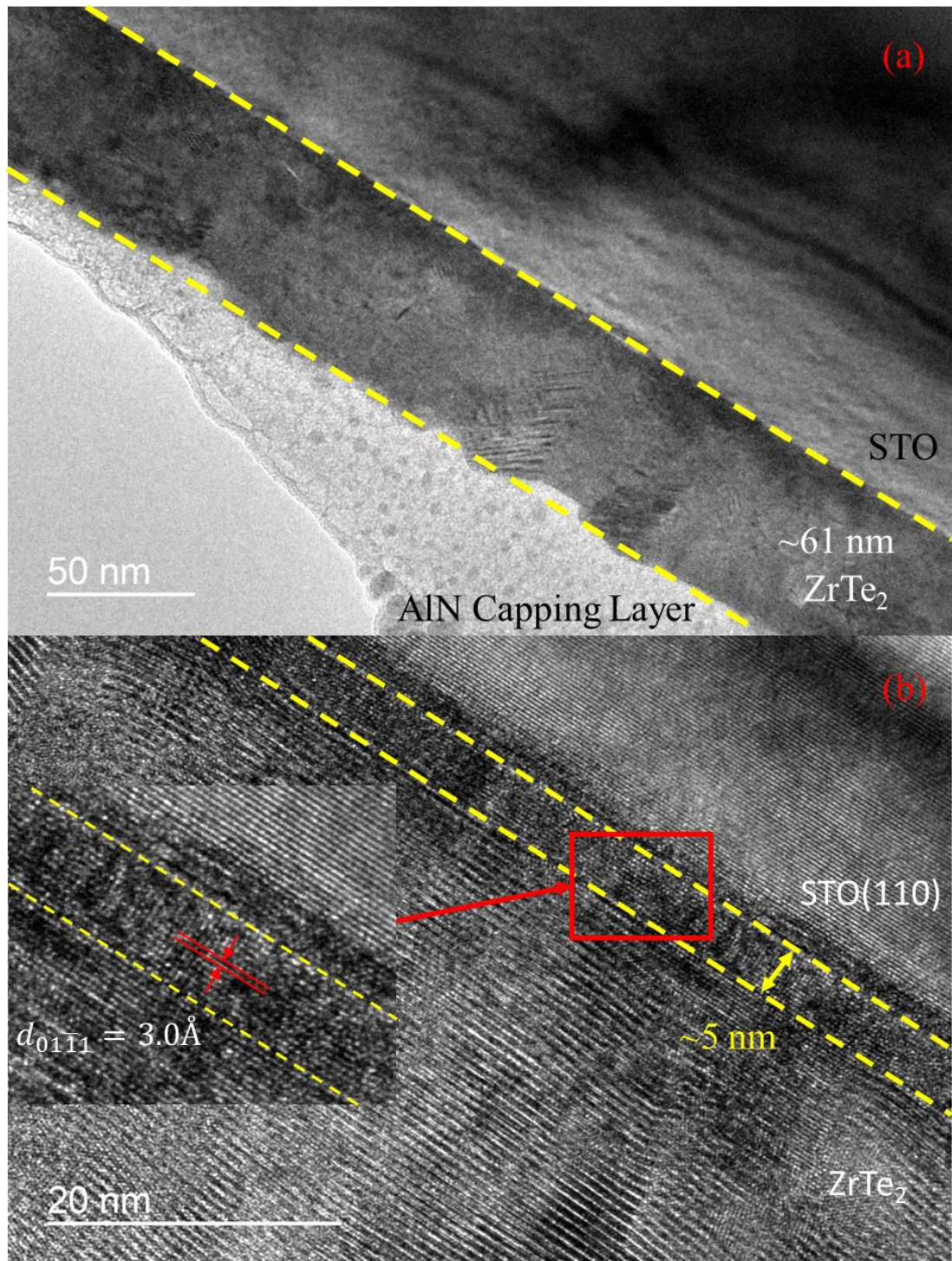
Figure 4-6. Electron Microscopy investigations of thin films grown on STO (110) at 550 °C.

(a) Low-magnification cross-sectional TEM image (b) High-magnification cross-sectional

TEM image. (Prepared using Ion Milling)

Due to the scale limitation of FIB technology, the thickness of the TEM sample usually cannot reach down to 100 nm, which affect the resolution of the TEM images. Compared to FIB technology, ion milling with relatively low milling rate and large milling area usually can produce a thinner TEM sample. So, a TEM specimen from the same thin film sample was prepared using mechanical polishing and ion milling. As we mentioned above that $ZrTe_2$ thin films are extremely sensitive to water, the sample was immersed inside ethanol during mechanical polishing process.

Figure 4-6 (b) shows the high-resolution images of the TEM sample prepared by ion milling, where the obtained results are consistent to the pervious results. The thickness of $ZrTe_2$ thin films is nearly 60 nm where the measured d-spacing is mainly indicating $ZrTe_2$ (0001). A 5 nm thick thin film layer can also be found between the $ZrTe_2$ (0001) thin film and substrate, in which the measured d-spacing is also similar to the results that obtained in the previous TEM sample.

4.3 Electrical transport properties of thin film samples on (110) STO

4.3.1 ρ-T Characteristic
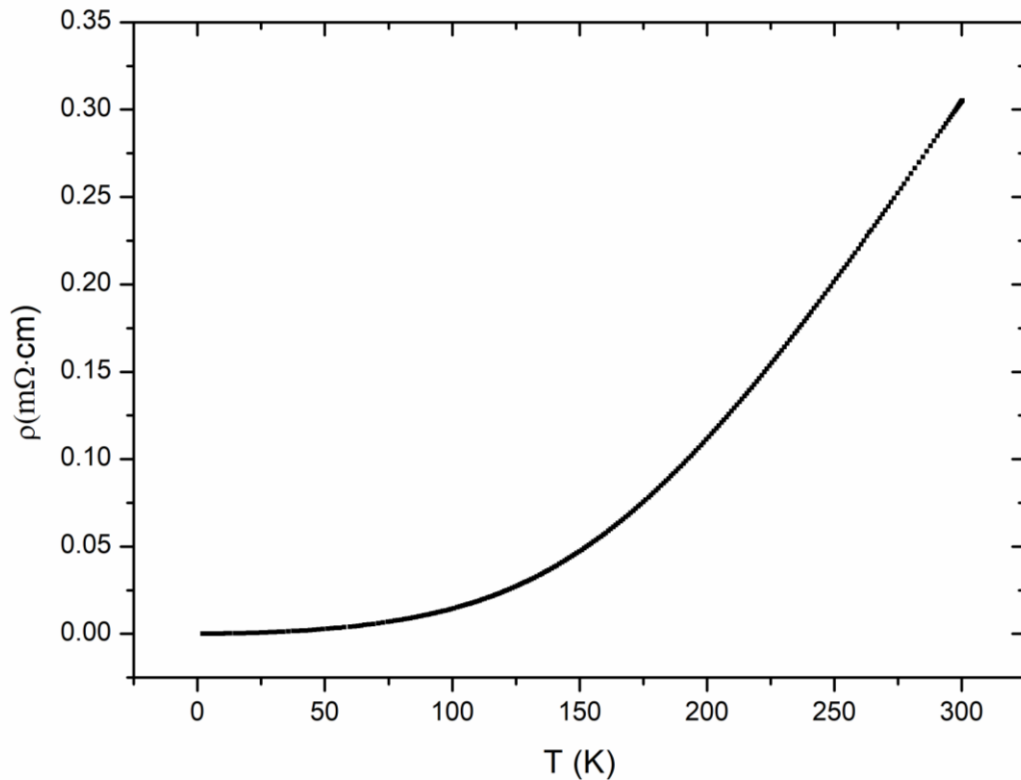
Figure 4-7. ρ-T Measurement of 550 °C thin film sample grown on STO.

The resistivity-temperature measurement was also conducted for some thin film samples grown on STO. Figure 4-7 shows the ρ-T measurement results of 550 °C thin film sample grown on STO, which is similar to the result from the ρ-T measurement in sapphire samples that ZrTe$_2$ thin films exhibiting typical metallic behavior in ρ-T measurement. But it should be pointed out that the resistance change from room temperature to 2 K is much more significant compared to that of the ZrTe$_2$ film on sapphire. This indicates that the film grown on (110) STO could have very different transport properties compared to the film grown on sapphire substrate.

4.3.2 Quasi-Two-Dimensional Nature
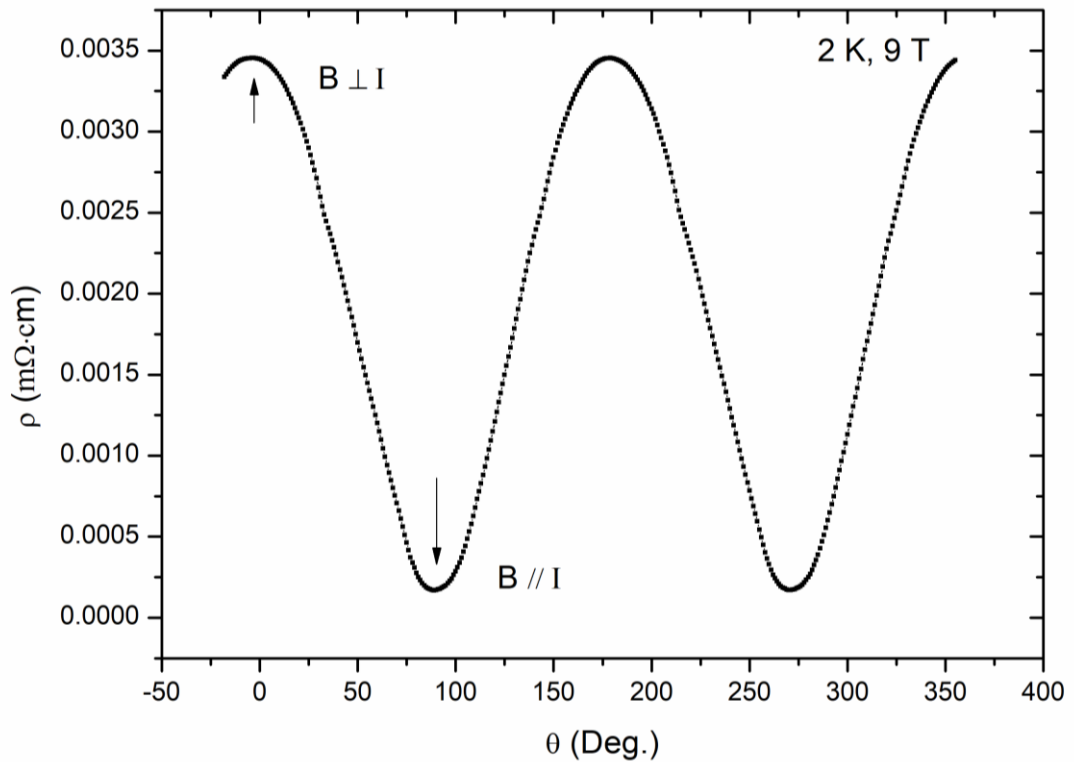
Figure 4-8. Angle-dependent MR for sample of 550 °C grown thin film on STO.

Figure 4-8 shows the angle-dependent MR measurement of thin film sample grown on STO at 550 °C. The resistivity shows maxima when the external magnetic field is perpendicular to the applied current, while it shows minima when the external magnetic field is parallel to the applied current. This magnetic field angle-dependency of the MR effect indicates the quasi-two-dimensional nature of the film on STO (110) substrate.d

4.3.3 MR and Hall measurement in perpendicular B field at different temperatures
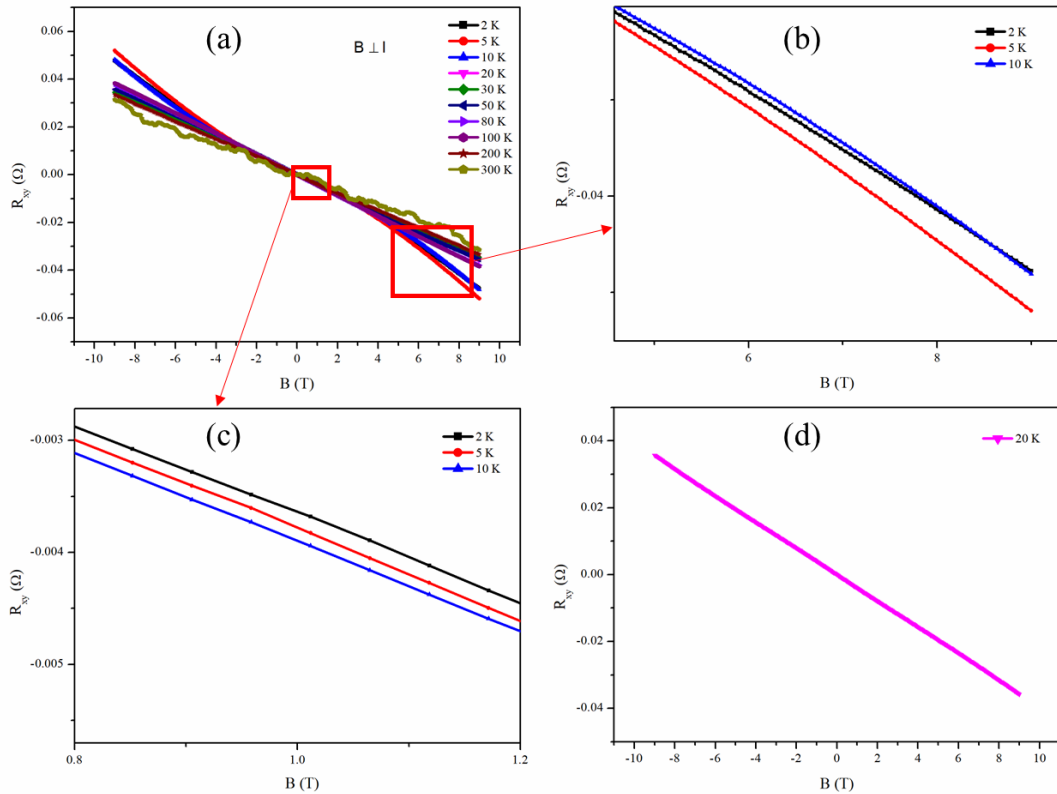
Figure 4-9. Temperature dependence of the Hall traces of 550 °C thin film sample grown on STO (a) from -9 T to 9 T at different temperature (b) nonlinear hall traces in large B under 10 K (c) linear hall traces in small B under 10 K, and (d) linear hall traces from -9 T to 9 T at 20 K.

Figure 4.9 (a) shows temperature dependence of the Hall traces for the 550 ºC grown thin film on STO. Different from the Hall traces in samples grown on sapphire substrate, in Figure 4-9 (b), nonlinear Hall traces are observed in large B under 10 K measurement, indicating the existence of multiple types carriers. While in Figure 4-9(c), linear Hall traces are observed in small B under 10 K measurement. It is also interesting to notice that, linear Hall traces is observed from -9 T to 9 T for measurement with sample

temperature above 20 K. (see Figure 4-9 (d))

Due to the linear Hall traces behavior in this sample in small B, the carrier density and mobility of dominant carrier at low temperature measurement can be estimated using the same method in 3.3.4. So, the estimated dominant carrier density is 2.62×10^{28} m^{-3}, 2.56×10^{28} m^{-3} and 2.60×10^{28} m^{-3}, for 2 K, 5 K and 20 K, respectively. And the estimated resistivity from the R-T measurement in 4.3.1 is 1.08×10^{-8} $\Omega \cdot$ m, 1.31×10^{-8} $\Omega \cdot$ m and 4.70×10^{-8} $\Omega \cdot$ m, for 2 K, 5 K and 20 K, respectively. Thus, the estimated dominant carrier mobility is 216 cm^2/Vs, 180 cm^2/Vs and 50 cm^2/Vs, for 2 K, 5 K and 20 K, respectively.
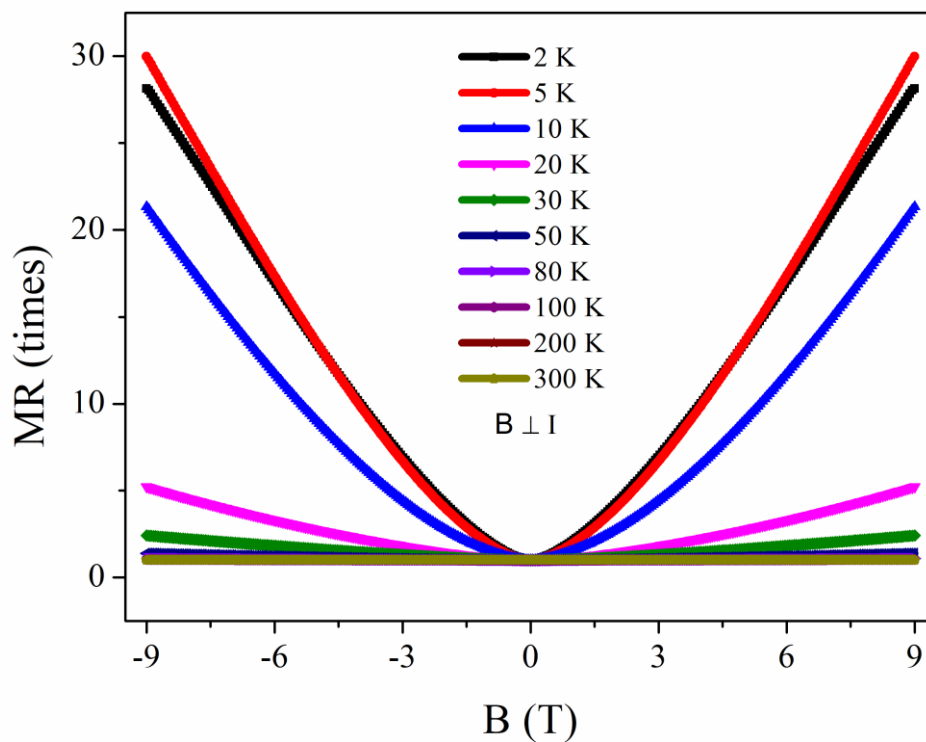
Figure 4-10. Temperature dependence of MR in B⊥ I.

Figure 4-10 shows temperature dependence of MR with B⊥I. One can see that at 2 K the Linear Magnetoresistance (LMR) is up to 30 times. Typically, the LMR effect can be observed in the Dirac semimetal and the origins of the LMR effect is not well defined.

For instance, in WTe_2, the extremely large MR is attributed to the compensation of holes and electrons; this explanation may also be applicable to our result.

In general, the MR effect is larger when the sample temperature is lower. However, in external magnetic field range from 4 T to 9 T, a slightly drop in the MR effect is found in measurement from 5 K to 2 K. Here we suggest two possible causes. One is the superconducting property of microscale indium ball used as electrode with critical temperature about 3.5 K. Another one is due to the existence of secondary carrier in the thin film sample. However, refers to the measured R-T characteristic at low temperature for this sample, the drop of resistivity cannot be found in the measurement at 2 K to 5 K; this indicates the negligible resistance of electrodes using Four-point probe method.

4.3.4 Negative MR with B // I at different temperature
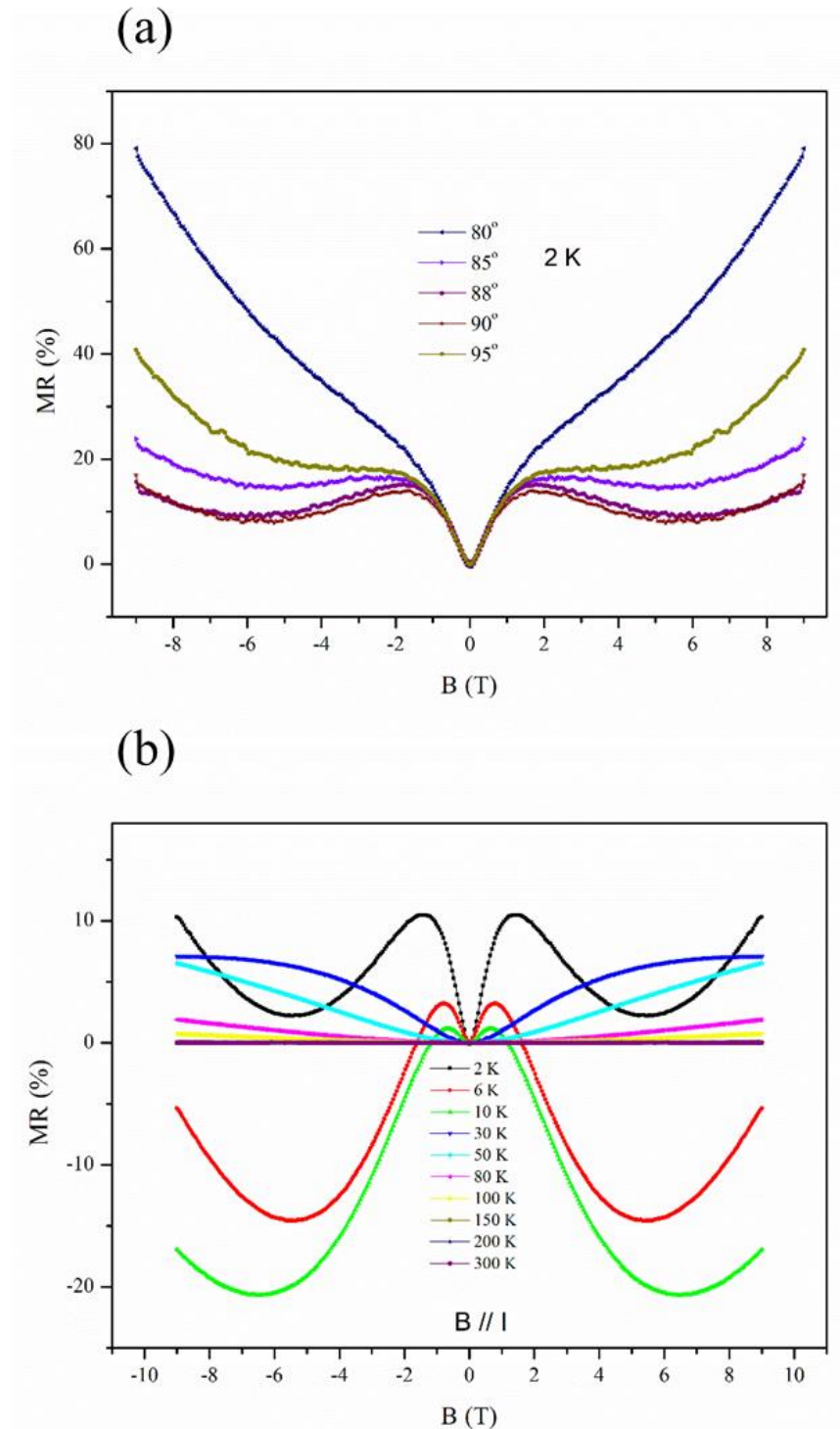
Figure 4-11. (a) Angular dependence of NMR, and (b) Temperature dependence of NMR

in B // I, for the sample of 550 ^{o}C thin film grown on STO.

From Figure 4-11 (b), NMR effect are observed in B // I at sample temperature lower than 10 K. The NMR effect may arise from many mechanisms, such as the chiral anomaly effect in the topological semimetal and the current jetting effect. The origin of the NMR effect observed in our samples is not well defined, further investigations should be done in the future. Besides, the angular dependence of NMR shows that the NMR is very sensitive to the angular relationship between external magnetic field and current while the NMR reach maximum at B // I (P = 90º).

4.3.5 Linear MR with B⊥I and B // film plane
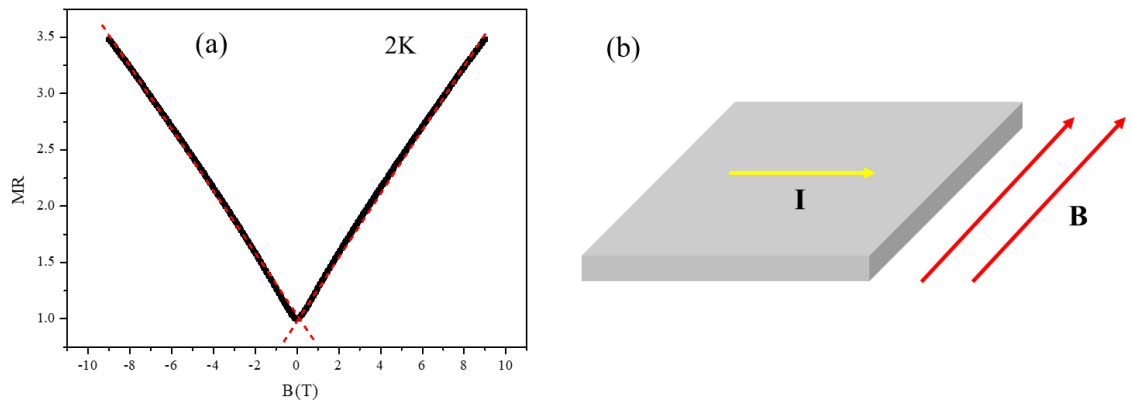
Figure 4-12. (a) MR-B Measurement in B ⊥ I and B // film plane at 2 K. (b) Schematic

Diagram of direction of I and B.

Large linear MR effect up to 3.5 times at 2 K & 9 T is observed in the MR-B measurement with B⊥I and B // film plane. The linear MR effect has long been discussed in several models, such as the Abrikosov's quantum linear model [60] and the inhomogeneous carrier model [61, 62]. However, the small carrier concentration claimed in the Abrkosov's quantum linear model shows contradiction to our measured large carrier density in Hall measurement; this means that this model cannot be applied in our case. Besides, similar phenomena was observed in the Weyl semimetal WTe_2 [63, 64], where linear MR effect was also observed in B ⊥ film under 4.2 K at 20 T. This model could be applicable to our sample, nevertheless, the origin of this is still not very clear.

4.4 Summary

For the ZrTe$_2$ thin films grown on (110) STO substrates, the main growth orientation is along [0001] direction, but the films present more defects and grains. There is also a thin interfacial layer which could be ZrTe$_2$ but with a different growth orientation along [01$\bar{1}$1] direction or a different phase of ZrTe. The thin film on STO (110) substrate show large MR when an external magnetic field is applied perpendicular to the film plane; while parallel magnetic field results in negative MR. More evidences suggest that the ZrTe$_2$ film on (110) STO substrate could be topological semimetal.

CHAPTER 5 Conclusion

In this thesis work, I have studied the deposition, structural characterization and transport measurements of the zirconium telluride thin films. The following conclusions can be made:

1. With $ZrTe_5$ target and by pulsed-laser deposition technique, $ZrTe_2$ films have been successfully deposited on different substrates. For (0001) sapphire substrate, due to the small lattice mismatch, epitaxial c-oriented $ZrTe_2$ thin films have been obtained. The $ZrTe_2$ films are in very good quality with a fixed orientation relationship with sapphire substrate, i.e., $(0001)_{ZrTe2}//(0001)_{Al2O3}$ and $[11\bar{2}0]$ $_{ZrTe2}//[01\bar{1}0]$ $_{Al2O3}$.

2. Within temperature range from 450 °C to 550 °C, highly c-oriented $ZrTe_2$ thin films have been grown on STO (110) substrate. However, different from the film on sapphire substrate, there is a clear interfacial layer of about 5 nm between the (0001) orientated ZrTe2 film and the (110) STO substrate. This interfacial layer is possibly ZrTe but may also be $ZrTe_2$ grown along $(01\bar{1}1)$ plane.

3. Optimized deposition for AlN capping layer has been achieved. This capping layer can effectively protect the $ZrTe_2$ film from reaction with air and can be used for other thin film capping layer for further study.

4. The $ZrTe_2$ thin film on sapphire substrate presents metallic transport characteristics within temperature range from 300 K to 2 K, and weak magnetoresistance can also be observed.

5. The thin film on STO (110) substrate also show typical R-T behavior of a metal or semi-metal, but with significant change of resistance from room temperature to

2 K low temperature. Moreover, large magnetoresistance is observed in the films when an external magnetic field is applied perpendicular to the film plane; while parallel magnetic field results in negative magnetoresistance. More evidences suggest that the $ZrTe_2$ film on (110) STO substrate could be topological semimetal.

Limitations of this research work and suggestions for future work

There are still a few questions remained in this thesis work. For example, the $ZrTe_2$ film on sapphire substrate shows higher quality of crystallinity and epitaxy. However, the transport property measurement results show only normal metal or semimetal without nontrivial characteristics. By contrast, the ZrT_2 film on STO substrate exhibit some nontrivial characteristics such as very large MR effect, negative MR effect and linear MR effect, suggesting topological semimetal nature of the film. These nontrivial characteristics could come from the interfacial layer which may be ZrTe phase. However, we cannot exclude the possibility that the interface is another growth direction of $ZrTe_2$. This is a problem remained and needs further study.

References

[1]   M. Acerce, D. Voiry, and M. Chhowalla, "Metallic 1T phase MoS$_2$ nanosheets as supercapacitor electrode materials," *Nat Nanotechnol,* vol. 10, no. 4, pp. 313-8, 2015.

[2]   J. Lee *et al.*, "Two-dimensional layered MoS$_2$ biosensors enable highly sensitive detection of biomolecules," *Sci Rep,* vol. 4, p. 7352, 2014.

[3]   A. K. Geim and I. V. Grigorieva, "Van der Waals heterostructures," *Nature,* vol. 499, no. 7459, pp. 419-25, 2013.

[4]   C. H. Lee *et al.*, "Atomically thin p-n junctions with van der Waals heterointerfaces," *Nat Nanotechnol,* vol. 9, no. 9, pp. 676-81, 2014.

[5]   W. Choi, N. Choudhary, G. H. Han, J. Park, D. Akinwande, and Y. H. Lee, "Recent development of two-dimensional transition metal dichalcogenides and their applications," *Materials Today,* vol. 20, no. 3, pp. 116-130, 2017.

[6]   B. A. Bernevig, Hughes, T. L., & Zhang, S. C. , "Quantum Spin Hall Effect and Topological Phase Transition in HgTe Quantum Wells," *Science,* vol. 314, no. 5806, pp. 1757-1761, 2006.

[7]   M. König, Wiedmann, S., Brüne, C., Roth, A., Buhmann, H., Molenkamp, L. W., ... & Zhang, S. C. , "Quantum Spin Hall Insulator State in HgTe Quantum Wells," *Science,* vol. 318, no. 5851, pp. 766-770, 2007.

[8]   X.-L. Qi and S.-C. Zhang, "The quantum spin Hall effect and topological insulators," *Physics Today,* vol. 63, no. 1, pp. 33-38, 2010.

[9]   S. Aminalragia-Giamini, J. Marquez-Velasco, P. Tsipas, D. Tsoutsou, G. Renaud, and A. Dimoulas, "Molecular beam epitaxy of thin HfTe$_2$ semimetal films," *2D Materials,* vol. 4, no. 1, 2016.

[10]   J. Jiang *et al.*, "Signature of type-II Weyl semimetal phase in MoTe$_2$," *Nat Commun,* vol. 8, p. 13973, 2017.

[11]   Y. Wu *et al.*, "Observation of Fermi arcs in the type-II Weyl semimetal candidate WTe$_2$," *Physical Review B,* vol. 94, no. 12, 2016.

[12]   H. Weng, X. Dai, and Z. Fang, "Transition-Metal Pentatelluride ZrTe$_5$ and HfTe$_5$: A Paradigm for Large-Gap Quantum Spin Hall Insulators," *Physical Review X,* vol. 4, no. 1, 2014.

[13]   W. Wang *et al.*, "Evidence for Layered Quantized Transport in Dirac Semimetal ZrTe$_5$," *Sci Rep,* vol. 8, no. 1, p. 5125, 2018.

[14]   T. M. Tritt, Lowhorn, N. D., Littleton IV, R. T., Pope, A., Feger, C. R., &

Kolis, J. W. , "Large enhancement of the resistive anomaly in the pentatelluride materials $HfTe_5$ and $ZrTe_5$ with applied magnetic field," *Physical Review B,* vol. 60, no. 11, p. 7816, 1999.

[15] X. Zhu *et al.*, "Superconductivity and Charge Density Wave in $ZrTe_{3-x}Se_x$," *Sci Rep,* vol. 6, p. 26974, 2016.

[16] P. Tsipas *et al.*, "Massless Dirac Fermions in $ZrTe_2$ Semimetal Grown on InAs(111) by van der Waals Epitaxy," *ACS Nano,* vol. 12, no. 2, pp. 1696-1703, 2018.

[17] E. H. Hall, "On a New Action of the Magnet on Electric Currents," *American Journal of Mathematics,* vol. 2, no. 3, pp. 287-292, 1839.

[18] K. v. Klitzing, G. Dorda, and M. Pepper, "New Method for High-Accuracy Determination of the Fine-Structure Constant Based on Quantized Hall Resistance," *Physical Review Letters,* vol. 45, no. 6, pp. 494-497, 1980.

[19] J. Schurr, F. Ahlers, and B. P. Kibble, "The ac quantum Hall resistance as an electrical impedance standard and its role in the SI," *Measurement Science and Technology,* vol. 23, no. 12, 2012.

[20] J. M. Charles Kane, "Topological insulators," *Physics World,* vol. 24, no. 2, 2011.

[21] B. I. Halperin, "Quantized Hall conductance, current-carrying edge states, and the existence of extended states in a two-dimensional disordered potential," *Physical Review B,* vol. 25, no. 4, p. 2185, 1982.

[22] C. L. Kane and E. J. Mele, "Quantum spin Hall effect in graphene," *Phys Rev Lett,* vol. 95, no. 22, p. 226801, 2005.

[23] P. Karnati, A. Haque, M. Taufique, and K. Ghosh, "A Systematic Study on the Structural and Optical Properties of Vertically Aligned Zinc Oxide Nanorods Grown by High Pressure Assisted Pulsed Laser Deposition Technique," *Nanomaterials,* vol. 8, no. 2, 2018.

[24] J. Schou, "Physical aspects of the pulsed laser deposition technique: The stoichiometric transfer of material from target to film," *Applied Surface Science,* vol. 255, no. 10, pp. 5191-5198, 2009.

[25] S. Amoruso, A. Sambri, and X. Wang, "Propagation dynamics of a La Mn O 3 laser ablation plume in an oxygen atmosphere," *Journal of applied physics,* vol. 100, no. 1, p. 013302, 2006.

[26] D. B. Geohegan and A. A. Puretzky, "Dynamics of laser ablation plume penetration through low pressure background gases," *Applied Physics Letters,* vol. 67, no. 2, pp. 197-199, 1995.

[27] C. Phipps, *Laser ablation and its applications*. Springer, 2007.

[28] J. Siegel, G. Epurescu, A. Perea, F. Gordillo-Vázquez, J. Gonzalo, and C. Afonso, "Temporally and spectrally resolved imaging of laser-induced plasmas," *Optics letters,* vol. 29, no. 19, pp. 2228-2230, 2004.

[29] S. Amoruso, R. Bruzzese, N. Spinelli, R. Velotta, M. Vitiello, and X. Wang, "Dynamics of laser-ablated MgB 2 plasma expanding in argon probed by optical emission spectroscopy," *Physical Review B,* vol. 67, no. 22, p. 224503, 2003.

[30] S. Amoruso, B. Toftmann, and J. Schou, "Thermalization of a UV laser ablation plume in a background gas: From a directed to a diffusionlike flow," *Physical Review E,* vol. 69, no. 5, p. 056403, 2004.

[31] H. Le, D. Zeitoun, J. Parisse, M. Sentis, and W. Marine, "Modeling of gas dynamics for a laser-generated plasma: Propagation into low-pressure gases," *Physical Review E,* vol. 62, no. 3, p. 4152, 2000.

[32] Y. Nakata, W. K. Kumuduni, T. Okada, and M. Maeda, "Plume-substrate interaction in pulsed-laser deposition of high-temperature superconducting thin films," *Applied physics letters,* vol. 64, no. 19, pp. 2599-2601, 1994.

[33] J. M. Warrender and M. J. Aziz, "Kinetic energy effects on morphology evolution during pulsed laser deposition of metal-on-insulator films," *Physical Review B,* vol. 75, no. 8, p. 085433, 2007.

[34] B. Thestrup, B. Toftmann, J. Schou, B. Doggett, and J. Lunney, "Ion dynamics in laser ablation plumes from selected metals at 355 nm," *Applied surface science,* vol. 197, pp. 175-180, 2002.

[35] P. Willmott and J. Huber, "Pulsed laser vaporization and deposition," *Reviews of Modern Physics,* vol. 72, no. 1, p. 315, 2000.

[36] S. Anisimov, D. Bäuerle, and B. Luk'Yanchuk, "Gas dynamics and film profiles in pulsed-laser deposition of materials," *Physical Review B,* vol. 48, no. 16, p. 12076, 1993.

[37] Y. B. Zel'Dovich and Y. P. Raizer, *Physics of shock waves and high-temperature hydrodynamic phenomena*. Courier Corporation, 2012.

[38] R. K. Singh and J. Narayan, "Pulsed-laser evaporation technique for deposition of thin films: Physics and theoretical model," *Physical Review B,* vol. 41, no. 13, p. 8843, 1990.

[39] M. Strikovski and J. H. Miller Jr, "Pulsed laser deposition of oxides: Why the optimum rate is about 1 Å per pulse," *Applied physics letters,* vol. 73, no. 12, pp. 1733-1735, 1998.

[40] R. Wood, K. Chen, J. Leboeuf, A. Puretzky, and D. Geohegan,

"Dynamics of plume propagation and splitting during pulsed-laser ablation," *Physical Review Letters,* vol. 79, no. 8, p. 1571, 1997.

[41]   S. Amoruso, B. Toftmann, and J. Schou, "Broadening and attenuation of UV laser ablation plumes in background gases," *Applied surface science,* vol. 248, no. 1-4, pp. 323-328, 2005.

[42]   D. L. Smith, *Thin-film deposition: principles and practice*. McGraw-hill New York etc, 1995.

[43]   S. Fähler, K. Sturm, and H.-U. Krebs, "Resputtering during the growth of pulsed-laser-deposited metallic films in vacuum and in an ambient gas," *Applied Physics Letters,* vol. 75, no. 24, pp. 3766-3768, 1999.

[44]   S. Fähler, S. Kahl, M. Weisheit, K. Sturm, and H. Krebs, "The interface of laser deposited Cu/Ag multilayers: evidence of the 'subsurface growth mode'during pulsed laser deposition," *Applied surface science,* vol. 154, pp. 419-423, 2000.

[45]   J. Barnes, A. Petford-Long, A. Suárez-Garcıa, and R. Serna, "Evidence for shallow implantation during the growth of bismuth nanocrystals by pulsed laser deposition," *Journal of applied physics,* vol. 93, no. 10, pp. 6396-6398, 2003.

[46]   A. Suárez-García, J. Barnes, R. Serna, A. Petford-Long, C. Afonso, and D. Hole, "The Shallow Implantation of Bismuth During the Growth of Bismuth Nanocrystals in Al 2 O 3 by Pulsed Laser Deposition," *MRS Online Proceedings Library Archive,* vol. 780, 2003.

[47]   A. Koma, K. Sunouchi, and T. Miyajima, "Fabrication and characterization of heterostructures with subnanometer thickness," *Microelectronic Engineering,* vol. 2, no. 1-3, pp. 129-136, 1984.

[48]   A. Koma, K. Sunouchi, and T. Miyajima, "Fabrication of ultrathin heterostructures with van der Waals epitaxy," AVS, 1985.

[49]   B. Parkinson, F. Ohuchi, K. Ueno, and A. Koma, "Periodic lattice distortions as a result of lattice mismatch in epitaxial films of two-dimensional materials," *Applied physics letters,* vol. 58, no. 5, pp. 472-474, 1991.

[50]   A. Koma, "Van der Waals epitaxy for highly lattice-mismatched systems," *Journal of crystal growth,* vol. 201, pp. 236-241, 1999.

[51]   A. Rigort and J. M. Plitzko, "Cryo-focused-ion-beam applications in structural biology," *Archives of biochemistry and biophysics,* vol. 581, pp. 122-130, 2015.

[52]   H. Cao *et al.*, "Quantized Hall Effect and Shubnikov–de Haas oscillations

in highly doped Bi_2Se_3: evidence for layered transport of bulk carriers," *Physical review letters,* vol. 108, no. 21, p. 216803, 2012.

[53]   Z. Xiong, D. Wu, Z. V. Vardeny, and J. Shi, "Giant magnetoresistance in organic spin-valves," *Nature,* vol. 427, no. 6977, p. 821, 2004.

[54]   A. D. W. F. K. McTaggart, "The Sulphides, Selenides, and Tellurides of titanium, zirconium, hafnium, and thorium," *Australian J. Chem,* vol. 11, no. 445, p. 57, 1958.

[55]   F. D. Jenkins, "A study of the solid regions in the system Zr-Te," 1972.

[56]   R. Grill *et al.*, "High-temperature defect structure of Cd-and Te-rich CdTe," *IEEE Transactions on Nuclear Science,* vol. 49, no. 3, pp. 1270-1274, 2002.

[57]   K. Yokota, S. Katayama, and T. Yoshikawa, "Thermally-Stimulated Current in p-Type CdTe Annealed in Various Atmospheres," *Japanese Journal of Applied Physics,* vol. 21, no. 3R, p. 456, 1982.

[58]   S. Li, M. S. Sellers, C. Basaran, A. J. Schultz, and D. A. Kofke, "Lattice strain due to an atomic vacancy," *International journal of molecular sciences,* vol. 10, no. 6, pp. 2798-2808, 2009.

[59]   Y. Luo *et al.*, "Hall effect in the extremely large magnetoresistance semimetal WTe_2," *Applied Physics Letters,* vol. 107, no. 18, p. 182411, 2015.

[60]   A. A. Abrikosov, L. P. Gorkov, and I. E. Dzyaloshinski, *Methods of quantum field theory in statistical physics*. Courier Corporation, 2012.

[61]   R. L. Petritz, "Theory of an experiment for measuring the mobility and density of carriers in the space-charge region of a semiconductor surface," *Physical Review,* vol. 110, no. 6, p. 1254, 1958.

[62]   E. Hwang, S. Adam, and S. D. Sarma, "Carrier transport in two-dimensional graphene layers," *Physical review letters,* vol. 98, no. 18, p. 186806, 2007.

[63]   X.-C. Pan *et al.*, "Robust linear magnetoresistance in WTe_2," *arXiv preprint arXiv:1505.07968,* 2015.

[64]   Y. Zhao *et al.*, "Anisotropic magnetotransport and exotic longitudinal linear magnetoresistance in WTe_2 crystals," *Physical Review B,* vol. 92, no. 4, p. 041104, 2015.